POLITECNICO
MILANO 1863

SCUOLA DI INGEGNERIA INDUSTRIALE
E DELL'INFORMAZIONE

# Techno-Economic Assessment and Optimal Sizing of a High-Temperature Heat Pump Configuration for Geothermal District Heating Applications

Tesi di Laurea Magistrale in
Energy Engineering - Ingegneria Energetica

**Alice Rossi, 252786**

**Abstract:** The decarbonisation of the heating sector is a central challenge of the energy transition, and high-temperature heat pumps integrated into district heating networks offer a promising route to reducing greenhouse gas emissions. This work analyses the techno-economic feasibility of integrating a high-temperature heat pump into a geothermal system in the Isar Valley. Three cycle configurations are considered: a single-stage cycle, a single-stage cycle with internal heat exchanger (IHX), and a two-stage cascade. For each, a screening of low Global Warming Potential working fluids is performed together with the determination of the minimum compressor size required to cover the peak thermal demand. Performance is assessed through annual thermodynamic simulations under realistic operating conditions, complemented by a scalability analysis in which the installed heat pump power is progressively reduced and the residual load covered by an auxiliary natural gas boiler. The configurations are compared through thermodynamic and economic indicators, i.e the coefficient of performance, the annual energy consumption, the equivalent operating hours, the levelised cost of heat and the payback time. Among the configurations analysed, the single-stage cycle with internal heat exchanger exhibits the most favourable thermo-economic performance. Hydrocarbon refrigerants achieve the best overall results: isobutane yields the lowest preliminary LCOH of 77.5 €/MWh, with a design-point COP of 4.45 and an optimal recuperator temperature difference of 11 K, resulting from the trade-off between cycle efficiency improvement and additional investment costs. The economic analysis shows that the system LCOH minimum occurs at low sizing factors; however, when the LCOH, the share of renewable energy delivered to the network, and the equivalent operating hours are considered jointly, a sizing factor of approximately 0.6 represents the most advantageous compromise, enabling coverage of 89% of the annual thermal demand. A sensitivity analysis shows that the economically optimal heat pump size is governed by the gas-to-electricity price ratio, shifting towards larger sizes as gas becomes more expensive relative to electricity, while the selected sizing factor remains a robust compromise owing to the flatness of the LCOH curve.The discounted payback time confirms the same ranking, with the single-stage cycle with the IHX amortising the investment in 18 years under baseline energy prices, falling to roughly 5 years under carbon-priced conditions.

**Advisor:**
Prof. Dario Alfani

**Co-advisors:**
Prof. Christopher Schifflechner
Arianna Passamonti

**Academic year:**
2025-2026

**Key-words:** High-temperature heat pump, Low-GWP refrigerants, Compressor sizing, Techno-Economic Assessment, Levelised cost of heat (LCOH)

# Nomenclature

## Acronyms

| | |
|---|---|
| BOP | Balance of Plant |
| CAPEX | Capital Expenditure |
| COP | Coefficient of Performance |
| DHN/S | District Heating Network/ System |
| ETS | Emission Trading System |
| GHP | Geothermal Heat Pump |
| GWP | Global Warming Potential |
| HC | Hydrocarbon |
| HCFO | Hydrochlorofluoroolefin |
| HEX | Heat Exchanger |
| HFC | Hydrofluorocarbon |
| HFO | Hydrofluoroolefin |
| HP | Heat Pump |
| HS | High Stage |
| HTHP | High-Temperature Heat Pump |
| IHX | Internal Heat Exchanger (recuperator) |
| LCOH | Levelized Cost of Heat |
| LS | Low Stage |
| PBT | Payback time |
| ODP | Ozone Depletion Potential |
| OPEX | Operational Expenditure |
| SG | Safety Group |
| SS | Single Stage |
| VDI | Verein Deutscher Ingenieure |
| VHC | Volumetric Heating Capacity |
| WF | Working Fluid |

## Refrigerants

| | |
|---|---|
| R290 | Propane |
| R600 | Butane |
| R600a | Isobutane |

## Physical quantities

| | |
|---|---|
| $AN$ | Total annuity, €/y |
| $C$ | Cost, € |
| $c$ | Specific cost, €/MWh |
| COP | Coefficient of performance |
| $f_{HP}$ | Heat pump sizing factor |
| $h$ | Specific enthalpy, J/kg |
| $\dot{m}$ | Mass flow rate, kg/s |
| $n$ | Shaft rotation speed, rpm |
| $n$ | Scaling exponent |
| $p$ | Pressure, bar |
| $P$ | Power, MW |
| $Q$ | Thermal energy, MWh |
| $\dot{Q}$ | Thermal power, MW |

## Physical quantities

| | |
|---|---|
| $s$ | Specific entropy, J/(kg K) |
| $T$ | Temperature, K or °C |
| $\Delta T$ | Temperature difference, K |
| $V$ | Volume, $m^3$ |
| $V_s$ | Compressor swept volume, $m^3$ |
| $w_{LS}$ | Cascade weighting factor |
| $x$ | Vapor quality |
| $X$ | Cost scaling parameter |
| $\eta$ | Efficiency |
| $\rho$ | Density, $kg/m^3$ |

## Subscripts

| | |
|---|---|
| boiler | Auxiliary boiler |
| brine | Geothermal brine |
| cascade | Cascade heat exchanger |
| comp | Compressor |
| cond | Condensation |
| DHN | District heating network |
| DHS | District heating supply |
| el | Electrical |
| eva | Evaporation |
| fluid | Working fluid |
| HP | Heat pump |
| HS | High stage |
| $i$ | Component / iteration index |
| IHX | Internal heat exchanger |
| in | Inlet |
| is | Isentropic |
| lift | Temperature lift |
| LS | Low stage |
| out | Outlet |
| pp | Pinch point |
| rec | Recuperator |
| sat | Saturation |
| shaft | Compressor shaft |
| sh | Superheating |
| sub | Subcooling |
| switch | Intermediate (cascade) level |
| sys | System |
| th | Thermal |
| w | Weighted |
| wf | Working fluid |

## Superscripts

| | |
|---|---|
| opt | Optimal value |

# 1. Introduction

The global energy sector faces one of the most pressing challenges of our time: the reduction of greenhouse gas emissions to limit the extent of global warming. The Paris Agreement of 2015 established the target of restricting the increase in global mean temperature to 1.5 °C above pre-industrial levels, committing signatory nations to deep and structural decarbonisation pathways [1].

In this context, the heating and cooling sector plays a strategic role: it accounts for approximately 26% of the total final energy consumption in Germany, and in 2023 as much as 70.3% of the national thermal energy demand was still met by fossil fuels [2].
Decarbonising this sector is therefore a priority, and low-emission technologies such as heat pumps are widely recognized as key enablers for the integration of renewable energy sources into district heating networks, a sector with significant abatement potential [3].
Heat pumps are thermodynamic machines capable of upgrading low-grade heat with a limited consumption of electrical energy [4]. In particular, high-temperature heat pumps, able to deliver supply temperatures up to 100 °C [5], are well suited for integration with district heating networks, enabling the exploitation of renewable heat sources such as geothermal energy. District heating networks, in turn, represent a well-established and efficient solution for the centralized distribution of thermal energy, characterized by high reliability and compatibility with a low-carbon energy supply [6, 7].
The relevance of these technologies is further underscored by the recent regulatory framework: the entry into force of the Heat Planning Act in Germany in 2024 [8] requires municipalities to develop local heating plans, within which geothermal energy is emerging as a priority renewable source in regions with high resource potential.

In recent years, several studies have investigated the integration of high-temperature heat pumps into district heating and geothermal systems, addressing thermodynamic performance, refrigerant selection, and techno-economic feasibility.
Jeßberger et al. [9] investigated the integration of large-scale heat pumps into deep geothermal heating plants through annual techno-economic simulations based on experimentally measured boundary conditions, evaluating the influence of operating conditions on the levelised cost of heat and addressing the maximization of the thermal output of existing installations. The methodology was shown to be transferable to other geothermal sites.
Kaufmann et al. [10] analyzed reversible high-temperature heat pumps for peak-load coverage in geothermal district heating systems, comparing their economic performance against conventional gas boilers and standard heat pumps under realistic part-load conditions derived from an existing plant. For 2022 energy prices, the gas boiler achieved the lowest levelised cost of heat (99.9 €/MWh), while the reversible heat pump, reached 145.4 €/MWh and overtook the standard high-temperature heat pump (150.4 €/MWh). Gas boilers were found to be favorable at low gas prices, whereas high-temperature and reversible heat pumps become economically competitive as gas price increase.
Arslan et al. [11] developed an optimization framework for geothermal district heating systems integrating thermal energy storage and heat pumps, conducting multi-objective parametric optimization over refrigerant selection and phase change material properties, complemented by exergo-economic and exergo-environmental analyses.
Deng et al. [12] investigated medium-depth geothermal borehole systems coupled with heat pumps for supply temperatures up to 55 °C, providing insight into the influence of system configuration and control strategy on overall performance for shallower geothermal resources.
Concerning advanced cycle configurations, Mateu-Royo et al. [13] compared eight high-temperature heat pump architectures combined with nine low-GWP refrigerants at a heat sink temperature of 130 °C, demonstrating that the optimal configuration is strongly dependent on the temperature lift. Two-stage arrangements were found to outperform single-stage ones for temperature lifts above 60 K, while all advanced configurations achieved a lower carbon footprint compared to conventional natural gas boilers, with equivalent $CO_2$ savings of up to 68%. Mota-Babiloni et al. [14] further investigated cascade systems equipped with internal heat exchangers, identifying pentane/butane as the fluid pair yielding the highest COP (3.15 at a heat sink temperature of 145 °C and a 60 °C heat source, a 13% improvement over the HFC-245fa/HFC-134a baseline) and confirming the suitability of hydrocarbon-based combinations for large temperature lifts.
On the refrigerant side, Arpagaus et al. [4] provided a comprehensive review of high-temperature heat pump technology, covering cycle performance and refrigerant suitability for supply temperatures above 90 °C, and identified the most promising low-GWP candidates for this application. Kosmadakis et al. [15] conducted a detailed techno-economic assessment of low-GWP refrigerants for waste-heat upgrading at temperatures up to 150 °C, showing that two-stage cycles outperform single-stage configurations both thermodynamically and economically at high temperature lifts, with payback periods as short as three to four years for large installations

operating with a temperature lift of 40 K.
From an economic standpoint, Schlosser et al. [5] reviewed the feasibility of large-scale heat pumps for supply temperatures up to 100 °C, classifying 155 implementations and highlighting the strong dependence of profitability on energy prices and annual operating hours. Consistent conclusions were reported by Jeßberger et al. [9] and Kaufmann et al. [10] in the geothermal context, where electricity price levels and full-load equivalent hours were identified as the primary economic drivers.

Although the literature provides extensive coverage of geothermal heat pump integration, advanced cycle architectures, and refrigerant selection, a systematic techno-economic comparison of multiple configurations under identical boundary conditions is still lacking. Most studies address either a single cycle topology, a restricted set of working fluids, or design-point calculations rather than full annual simulations. In particular, no prior work has conducted an annual thermo-economic comparison of a single-stage cycle, a single-stage cycle with internal heat exchanger, and a cascade cycle for the same real geothermal district heating application, with simultaneous refrigerant screening and compressor sizing optimization. The present work addresses this gap through annual simulations of a real geothermal district heating plant in the Isar Valley, evaluating the three configurations across a selection of low-GWP refrigerants within a unified LCOH-based framework.

## 1.1. Objective of the thesis

The objective of the present work is to perform a techno-economic feasibility analysis of a large-scale high-temperature heat pump integrated into a geothermal district heating system, with the aim of identifying the optimal configuration under realistic operating boundary conditions.

To this end, three cycle architectures are investigated: a single-stage cycle, a single-stage cycle with internal heat exchanger, and a two-stage cascade configuration. For each of them, a screening of low-GWP working fluids is performed and the minimum compressor size required to cover the peak thermal demand of the network is determined.

A parametric analysis is subsequently carried out, in which the heat pump installed sizing factor is progressively reduced and the residual thermal load is assigned to an auxiliary natural gas boiler, with the objective of identifying the optimal system sizing.

The configurations are finally compared both thermodynamic-wise and economic-wise through the evaluation of key performance indicators, including the coefficient of performance (COP), the annual electrical energy consumption, the equivalent full-load operating hours, and the levelised cost of heat (LCOH).

# 2. System Description

## 2.1. Reference System

The heat source of the system under analysis is the geothermal brine extracted from the Molasse Basin, one of the largest hydrothermal reservoirs in Germany, situated in the Isar Valley. The plant comprises two extraction wells and one reinjection well [16], the latter positioned 2 km from the extraction wells to promote natural thermal recovery of the fluid within the formation, at an average depth of 4000 m, which classifies the resource as deep geothermal [17]. The geothermal production system, the primary heat exchanger, the district heating network, and the auxiliary natural gas boiler are regarded as predefined system components and are therefore not subject to redesign within the scope of this work. The objective of the present study is exclusively the thermo-economic sizing and assessment of the high-temperature heat pump to be integrated into this existing infrastructure.
Geothermal energy plays a relevant role in the Bavarian renewable energy mix, as a matter of fact the current geothermal heating capacity in Bavaria alone amounts to approximately 1510 GWh of heat per year, corresponding to roughly 3% of the total renewable energy production in the region [18].
The extracted brine reaches the surface at temperatures ranging from 90 °C to 110 °C, with a total mass flow rate of 81.5 kg/s. Following the primary heat exchanger, the brine enters the heat pump cycle at 61.5 °C. To preserve the integrity of the geothermal reservoir and prevent thermal depletion of the source, the brine return temperature is maintained above 30 °C [19].
The primary function of the plant is to supply thermal energy to the district heating network (DHN) via the heat pump condenser, with a thermal output of 7.13 MW. District heating systems are conventionally structured around three subsystems: a generation system, responsible for centralized heat production; a distribution

system, consisting of a network of insulated supply and return pipes; and a consumption system, which delivers heat for space heating, domestic hot water, and process heat applications [20]. The network under consideration extends over 60 km and operates with a supply temperature ranging from 56.5 °C to 93.63 °C, at a mass flow rate of 62.77 kg/s [21]. The annual profiles of the DHS supply temperature and brine temperature, together with the corresponding mass flow rates, are reported in Figure 1 over the full period considered (April 2022 – March 2023).

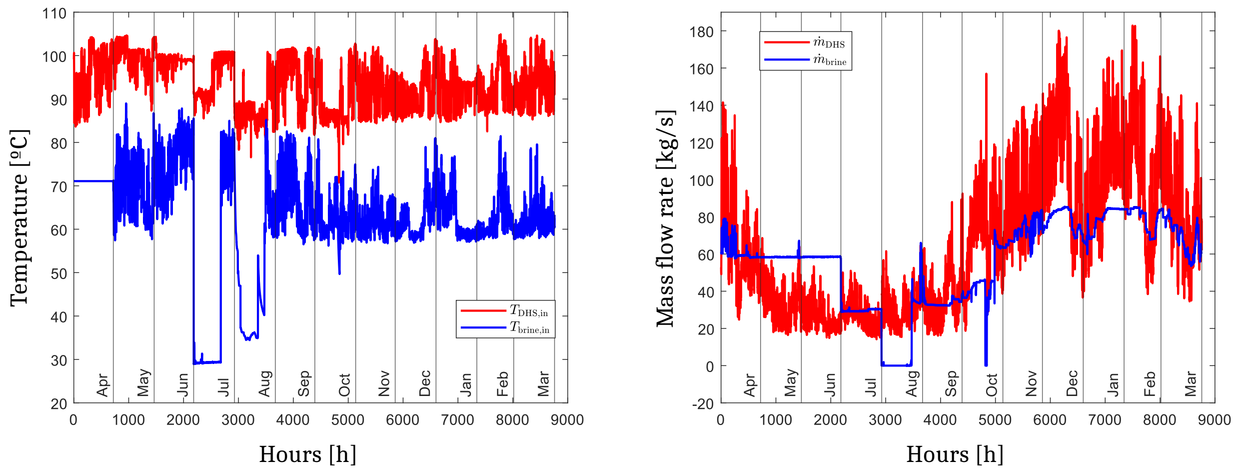


Figure 1: Annual profiles of the DHS supply and brine temperatures (left) and of the DHS and brine mass flow rates (right) over the period April 2022 – March 2023.

As illustrated in Figure 2, the system is supplemented by a natural gas boiler, which ensures full thermal coverage of the DHN demand during scheduled maintenance or in the event of plant failure, thereby guaranteeing continuity of service. The integration between the heat pump and the auxiliary boiler is also predefined. In particular, the split of the district heating supply (DHS) mass flow rate between the heat pump condenser and the auxiliary boiler is prescribed by the reference system model and constitutes a boundary condition throughout this work. Consequently, the mass flow distribution is not optimized, and the analysis focuses solely on the sizing and operation of the heat pump under these imposed operating conditions.

The annual load profile adopted in this work is derived from the measured heat demand of an existing geothermal heating plant in the same area, combined with hourly ambient temperature data for the Munich area, covering the period considered [21].

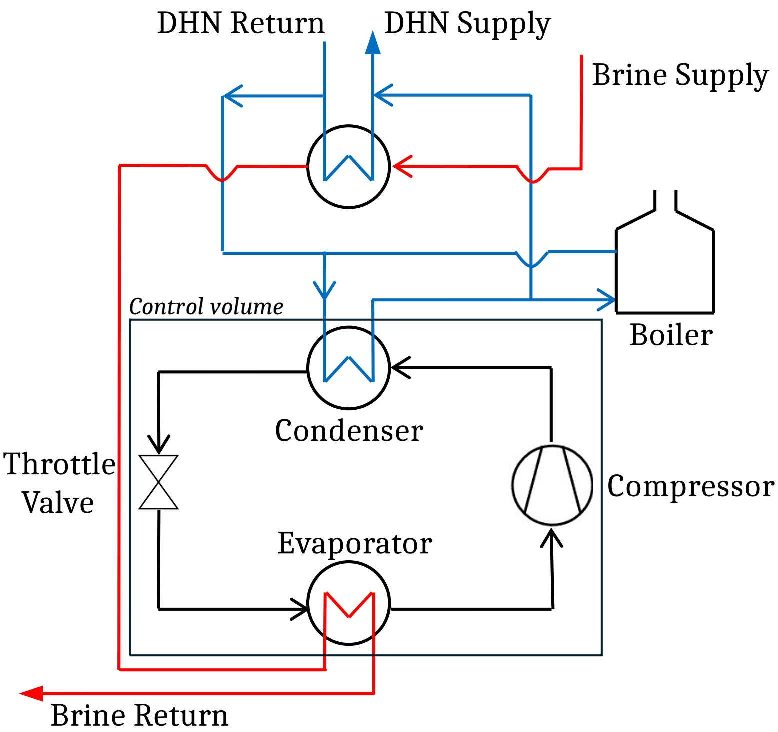


Figure 2: HTHP operation mode in a geothermal heat pump (GHP).

## 2.2. Heat pump configurations

Building on the findings of the literature reviewed above, three heat pump configurations have been analyzed in terms of their applicability to the system under consideration. The plant schematics and the temperature–specific entropy ($T$–$s$) diagrams of the respective cycle configurations are presented in Figure 3.
The single-stage configuration represents the baseline case. It consists of a compressor, a condenser, an expansion valve, and an evaporator; the latter is equipped with a superheating section. This arrangement ensures that the fluid enters the compressor as saturated or slightly superheated vapor, thereby preventing corrosion and erosion phenomena caused by liquid droplets inside the compressor, which may occur when compression takes place within the two-phase region.

The single-stage configuration with internal heat exchanger (IHX) introduces a recuperative heat exchanger, whose dual function is to superheat the vapor leaving the evaporator while simultaneously subcooling the saturated liquid exiting the condenser. This configuration is particularly suited to moderate temperature lifts, as the energy efficiency gains provided by the IHX become most pronounced when the temperature lift does not exceed approximately 40 K [22–25].

The two-stage cascade configuration consists of two separate vapor-compression cycles – a low-stage (LS) cycle and a high-stage (HS) cycle, each equipped with its own compressor, arranged in series with respect to the heat transfer chain. The two circuits are thermally coupled through a cascade heat exchanger, which acts as the condenser for the LS cycle and as the evaporator for the HS cycle. In both circuits, adequate superheating of the fluid at the evaporator outlet is ensured. This architecture is particularly advantageous at high temperature lifts, where two-stage compression has been shown to offer significant performance benefits over single-stage solutions, especially above 60 K [13].
A distinctive feature of cascade systems is the possibility of operating the two circuits with different working fluid combinations, offering greater flexibility in both design and performance optimization. In this work a physically motivated pairing strategy was adopted: fluids with a critical temperature below 120 °C, namely R290 and R1234yf, were assigned to the LS circuit, while fluids with a higher critical temperature were assigned to the HS circuit. All possible combinations between these two groups were then evaluated.

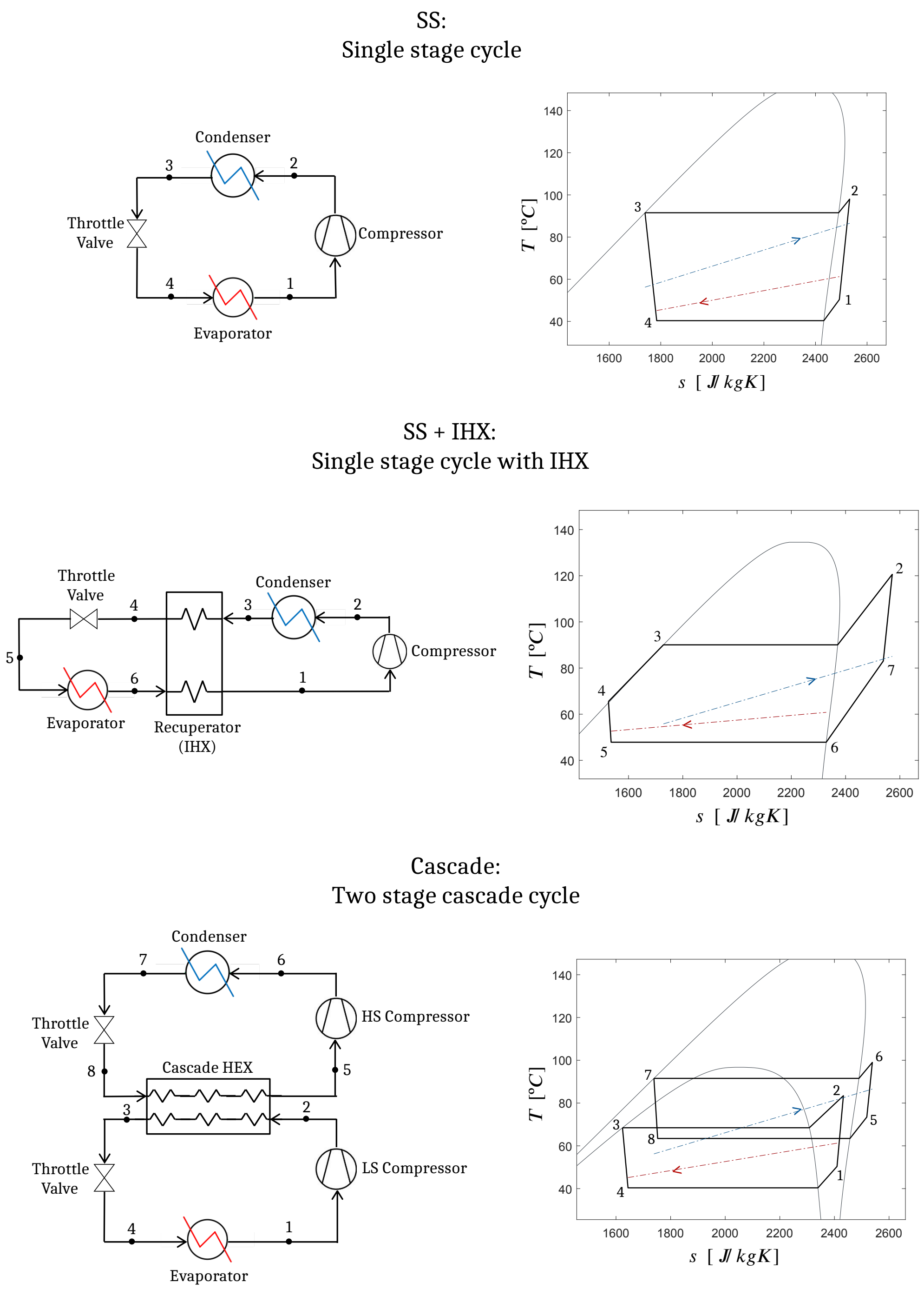


Figure 3: Schematic representations and T-s diagrams of the HTHP cycle configurations.

## 2.3. Refrigerants selection

The selection of the working fluid represents a key parameter in the design of a heat pump, as extensively discussed in the literature [26, 27].
In order to be suitable for this application, the refrigerant must satisfy several thermodynamic, environmental, and safety criteria.
Since this study focuses on the subcritical operation of a large-scale heat pump, the working fluid must exhibit a high critical temperature, with a condensing temperature at least 10–15 K below it. Furthermore, the critical pressure must not exceed 30 bar, so as to limit mechanical stress on system components [28], while the low-side pressure must remain above 1 bar to prevent air infiltration. The maximum fluid temperature must additionally be kept below 160 °C to ensure thermal stability of the refrigerant–oil mixture [4].
From an environmental standpoint, the use of ozone-depleting substances such as chlorofluorocarbons (CFCs) and hydrochlorofluorocarbons (HCFCs) has been progressively phased out under the Montreal Protocol, and their use is further prohibited in Europe by Regulation (EC) No 1005/2009 [29]. Hydrofluorocarbons (HFCs), which replaced them as the third generation of refrigerants, have in turn been subject to increasingly stringent restrictions: EU Regulation No 517/2014 [30] introduced a gradual phase-down of HFCs by imposing market consumption quotas and capping the maximum allowable GWP in specific applications, with the aim of accelerating the transition towards low-GWP alternatives. This regulatory framework prompted the emergence of the so-called fourth-generation refrigerants that present a null Ozone Depletion Potential (ODP) and a GWP below 10, so as to ensure regulatory compliance and long-term applicability. It is noted that, although certain hydrochlorofluoroolefins (HCFOs) contain chlorine, their ODP is considered negligible due to their short atmospheric lifetime [31].
Safety requirements further constrain the selection to non-toxic fluids with low flammability, in order to minimize the need for additional safety measures. Finally, the fluid must be commercially available at a competitive price.
In order to identify a suitable set of candidate refrigerants, the most promising results reported in the literature were also taken into account. Royo et al. [13] identified isobutane (R600a), propane (R290), and R1233zd(E) as the fluids offering the best trade-off between COP and volumetric heating capacity (VHC). The suitability of hydrocarbons as low-GWP alternatives to HFC-134a in vapor-compression applications has been further supported by Palm [32], who showed that R600a and R290 represent effective substitutes across a range of heat pump systems. Arpagaus et al. [4] reported optimal thermodynamic performance for R1234yf, a hydrofluoroolefin (HFO) whose viability as a drop-in replacement for HFC-134a has been demonstrated also in liquid chiller applications [33]. Babiloni et al. [14] investigated cascade configurations incorporating butane (R600).
Table 1 summarizes the final selection of working fluids together with their thermophysical properties, namely the critical point coordinates, GWP, ODP, safety class, and indicative market price [4].
The saturation curves of the selected refrigerants are shown in Figure 4 in the T–s and p–h planes. The critical temperatures span a wide range, from approximately 95 °C for R1234yf and R290 up to about 166 °C for R1233zd(E), directly reflecting the values listed in Table 1 and determining how close each fluid operates to its critical point at the required condensation temperature. The shape of the two-phase dome is instead governed by the molecular complexity of the fluid (broadly correlated with its molecular mass): heavier, more complex molecules such as R1233zd(E) and R1234ze(Z) exhibit an overhanging (positively-sloped) saturated-vapour curve, characteristic of dry/isentropic fluids, whereas the lighter hydrocarbons (R290, R600, R600a) display a more classical bell-shaped dome typical of wet fluids. The overhanging shape of the dry fluids limits the superheating attainable at the compressor inlet and motivates the adoption of the internal heat exchanger for these refrigerants, as discussed in Section 2.2. Finally, the p–h diagram highlights the marked differences in operating pressure levels among the candidates, with R290 exhibiting considerably higher saturation pressures than the butanes; this behaviour is consistent with the critical-pressure screening criterion ($p_c < 30$ bar) and explains the higher evaporation pressures reported for R290 in the Tables in section 4.1.

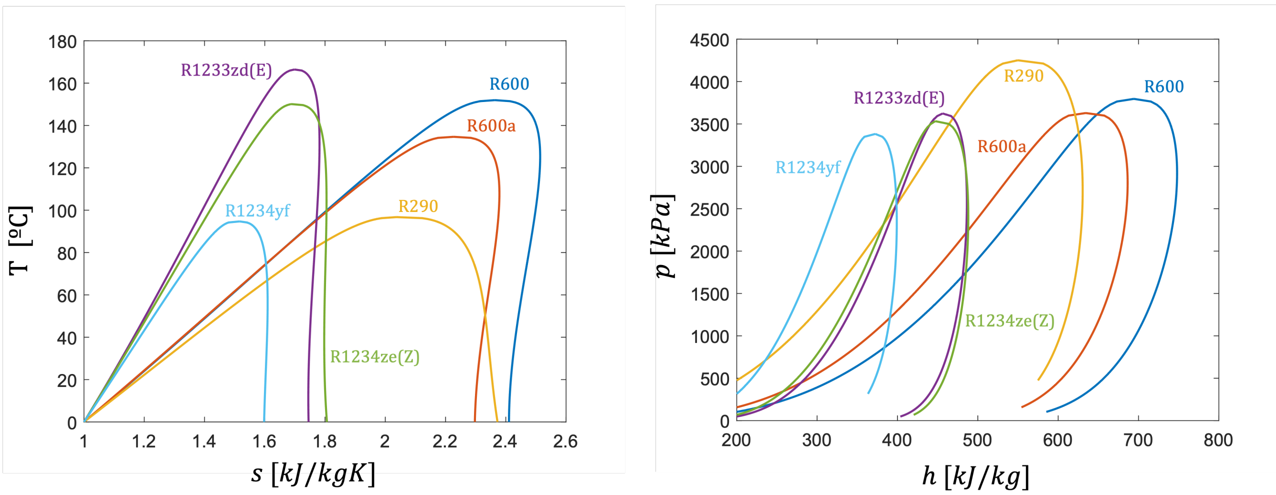


Figure 4: Saturation curves of the selected working fluids in the T–s (left) and p–h (right) diagrams.

The refrigerant screening differs slightly among the investigated configurations. Due to its relatively low critical temperature, R1234yf is excluded from the single-stage and single-stage with internal heat exchanger analyses, where the cycle would operate in excessive proximity to the critical point, leading to non-physical predictions from the economic model. It is, however, retained for the low-stage (LS) cycle of the cascade configuration.

Table 1: Selected working fluids and thermophysical properties.

| Type | Refrigerant | $T_c$ [°C] | $p_c$ [bar] | $MM$ [g/mol] | GWP | ODP | SG | Price [€/kg] |
|---|---|---|---|---|---|---|---|---|
| HFO | R1234yf | 94.7 | 33.8 | 114.0 | <1 | 0 | A2L | 20 |
| HC | Propane (R290) | 96.7 | 42.5 | 44.1 | 3 | 0 | A3 | 2 |
| HC | Isobutane (R600a) | 134.7 | 36.3 | 58.1 | 3 | 0 | A3 | 2 |
| HFO | R1234ze(Z) | 150.1 | 35.3 | 114.0 | <1 | 0 | A2L | 20 |
| HC | Butane (R600) | 152.0 | 38.0 | 58.1 | 4 | 0 | A3 | 2 |
| HCFO | R1233zd(E) | 166.5 | 36.2 | 130.5 | 1 | 0 | A1 | 35 |

# 3. Methodology

## 3.1. Overall Workflow

The methodology adopted to obtain the results for each configuration is described hereafter, a schematic representation of the procedure is provided in Figure 5.

The first parameter to be determined is the compressor swept volume $V_s$, which directly governs the sizing of the compressor. An adequate compressor sizing must ensure full coverage of the peak thermal demand of the DHN while avoiding over-dimensioning, which would result in unnecessarily high capital costs. To this end, $V_s$ is identified through an iterative procedure over a discrete range of values between $0.01\,\mathrm{m}^3$ and $0.09\,\mathrm{m}^3$, evaluated at the hourly time step corresponding to the most demanding operating condition, namely the peak load. The minimum value of $V_s$ that ensures complete peak demand coverage without requiring the intervention of the auxiliary boiler is then selected as the optimal compressor size.
Once the optimal swept volume has been identified, a full annual thermodynamic simulation is carried out, in order to characterize the heat pump behaviour across all operating conditions throughout the year. This procedure is repeated for each working fluid under consideration.

A scalability analysis is subsequently performed, in which the heat pump sizing factor is progressively reduced by imposing that it covers only a specified fraction of the peak load, with the remaining thermal demand met by the auxiliary boiler. For each working fluid and each coverage ratio, the swept volume is re-determined following the same procedure described above, and a new annual simulation is carried out accordingly.

A techno-economic analysis of the complete system (high-temperature HP + auxiliary boiler, if employed) is then conducted for each working fluid and each sizing factor, defined as the fraction of the peak load assigned to the heat pump. This analysis accounts not only for the heat pump itself, but also for the operating costs associated with the auxiliary boiler, primarily driven by natural gas consumption.

All scenarios are ultimately compared both thermodynamically and economically, with the objective of identifying, for each plant configuration, the most suitable working fluid together with the corresponding optimal swept volume and heat pump sizing.

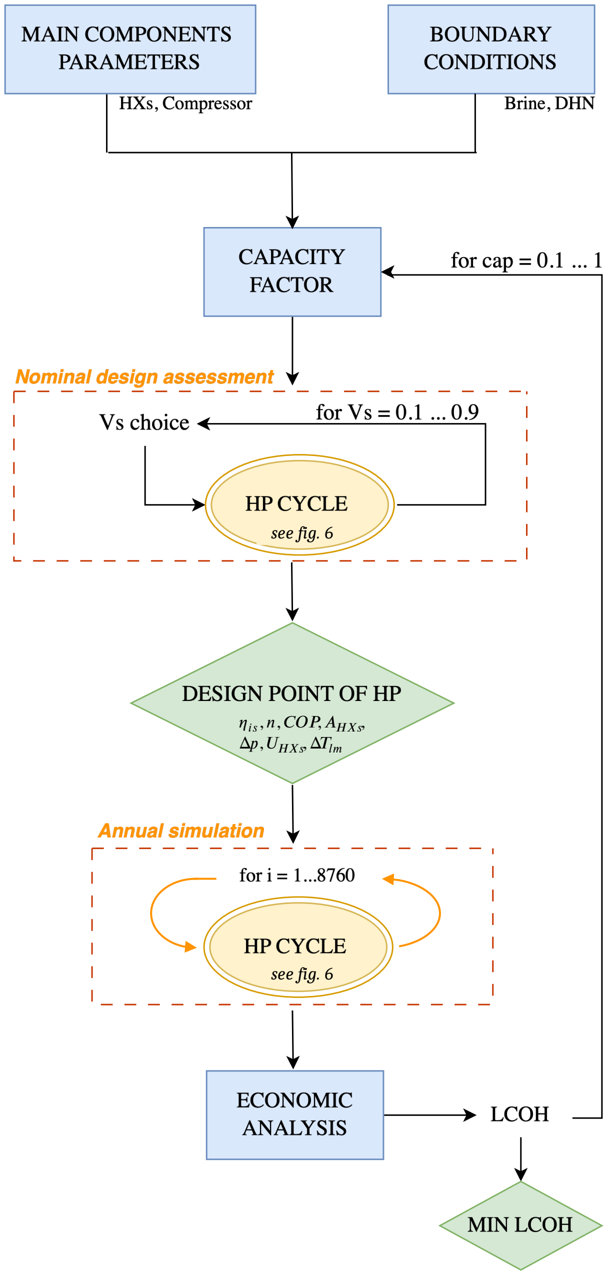


Figure 5: Methodology flow diagram.

## 3.2. Modeling assumptions

The model, based on the framework developed by Kaufmann et al. [10], implements the steady-state simulation of a high-temperature heat pump integrated into a district heating system. For each operating condition within the annual load profile, it constructs the boundary conditions of both the heat source and the thermal load. For the purpose of the thermodynamic calculations, both the geothermal brine and the district heating system (DHS) fluid are modeled as water. Consequently, the influence of dissolved minerals and salinity on the thermophysical properties of the brine is neglected. Thermophysical properties for all cycle calculations are

retrieved from REFPROP [34].
The model takes the following quantities as input. The boundary conditions, determined by the external system, are:

- supply and return temperature and pressure of the DHN;
- district heating mass flow rate assigned to the heat pump;
- brine temperature and pressure available at the evaporator inlet;
- brine mass flow rate.

The design parameters to be properly selected are:

- working fluid;
- superheating degree;
- compressor parameters.

The problem is formulated with two decision variables: the working fluid mass flow rate and the evaporation pressure. The objective is to minimize the mechanical power absorbed by the compressor while exactly meeting the thermal load demanded by the district heating network. The evaporation pressure is subject to the constraint that the evaporator pinch point must remain above 5 K, while the working fluid mass flow rate must be such that the compressor operates within the admissible speed range of 500 to 4500 rpm.

The compressor is modeled following the generalized low-order approach for twin-screw machines developed by Kaufmann et al. [35] and detailed in the appendix A, which yields the isentropic and volumetric efficiencies as a function of the swept volumetric flow rate and the pressure ratio. This allows the compressor rotational speed and shaft power to be determined, and enables realistic part-load modeling independently of the machine size and, to a large extent, of the built-in volume ratio.
The heat exchangers are modeled using a finite volume approach based on energy balances, adapted from the formulation proposed by Braimakis and Karellas [36]. A minimum pinch point of 5 K is imposed on all heat exchanger components and the pressure drops inside the heat exchangers are neglected in order to have isobaric processes.
The auxiliary natural gas boiler is modeled with a constant thermal efficiency of 90 %, which is assumed to be independent of the operating load throughout the analysis.
Throughout every simulation, and for all cycle configurations, it was verified at each operating point that the maximum temperature reached by the working fluid — attained at the compressor outlet, remained below the 160 °C limit imposed in Section 2.3 to ensure the thermal stability of the refrigerant–oil mixture. This constraint was satisfied across the entire annual load profile for all the retained refrigerants, confirming the thermal admissibility of the selected working fluids under the full range of operating conditions.
To reduce the computational effort associated with annual hourly simulations (8760 operating points), the hourly operating data are aggregated into a set of representative typical days according to the VDI 4655 [37]. Each typical day represents a group of real days with similar operating conditions and is assigned a weighting factor corresponding to the number of days it represents throughout the year. This approach preserves the seasonal variability of the thermal demand while significantly reducing the number of simulations required.
To carry out the scalability analysis introduced in Section 3.1, a reduced installed power is defined by means of a sizing factor.

$$f_{\mathrm{HP}} = \frac{\dot{Q}_{\mathrm{HP}}}{\dot{Q}_{\mathrm{nom}}} \tag{1}$$

where $f_{HP}$ is the HP sizing factor, $Q_{HP}$ is the load covered by the heat pump and $Q_{nom}$ is the nominal load equal to 7.13 MW.
The scalability analysis is performed to investigate the trade-off between the environmental and economic performance of the integrated heating system. Increasing the installed heat pump capacity allows a larger fraction of the annual thermal demand to be supplied from the geothermal heat pump, thereby reducing the reliance on the auxiliary natural gas boiler and moving the system closer to full decarbonization. However, a larger heat pump also entails higher capital investment and typically results in fewer equivalent full-load operating hours, leading to a lower utilization of the installed capacity. Conversely, reducing the installed heat pump capacity decreases the investment cost and increases the equivalent operating hours of the heat pump, but requires a greater contribution from the auxiliary boiler, resulting in higher natural gas consumption and associated $CO_2$ emissions. The scalability analysis therefore aims to identify the heat pump size that provides the most suitable compromise between economic performance, renewable heat supply, and emission reduction.

### 3.2.1 Single-stage configuration

The single-stage configuration constitutes the reference cycle for the heat pump system. Before solving the thermodynamic cycle, preliminary calculations are performed to define the heat-sink boundary conditions. The

condensation temperature is set equal to the DHS outlet temperature plus a minimum pinch-point difference of 5 K, from which the corresponding condensation pressure is obtained using the saturation properties of the selected refrigerant. The known DHS pressure and inlet and outlet temperatures are used to evaluate the specific enthalpy increase of the district heating water and, consequently, the thermal load required by the network. The cycle optimization then determines the heat pump working-fluid mass flow rate and the evaporation pressure that minimize the compressor power while meeting the required thermal load. The thermodynamic cycle solution is initiated at the expansion valve, where the working fluid, in a saturated liquid state, undergoes isoenthalpic expansion into the two-phase region. The fluid then enters the evaporator, where it completes the phase transition reaching the saturated vapor state; the final section of the component is the superheater, which provides a superheating degree of $\Delta T_{sh} = 10\,\mathrm{K}$, bringing the fluid to a superheated vapor condition.
The superheated vapor is subsequently compressed, reaching the highest temperature of the cycle at the compressor outlet. It then enters the condenser, where it is first de-superheated to the saturated vapor state and subsequently condensed back to saturated liquid, completing the cycle.

A detailed description of the thermodynamic cycle, including the derivation of the thermodynamic states, thermal and mechanical power outputs, compressor efficiencies, and the resulting COP, is provided in Figure 6.

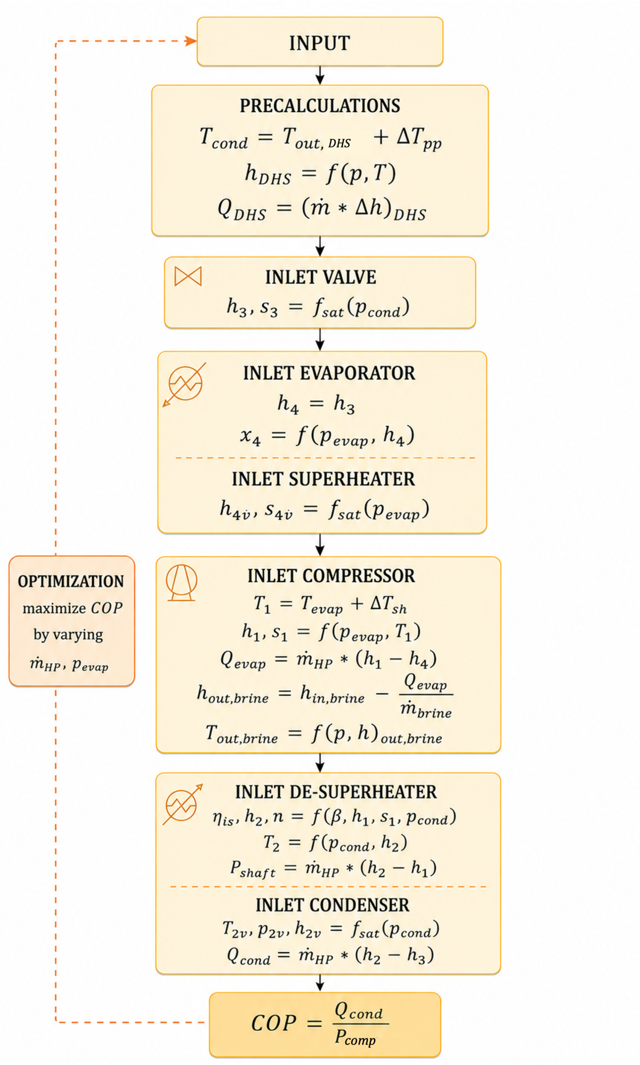


Figure 6: Numerical solving approach for HTHP.

### 3.2.2 Single-stage configuration with internal heat exchanger

The single-stage cycle with internal heat exchanger (IHX) differs from the reference configuration by the addition of a recuperative heat exchanger between the low-pressure and high-pressure sides of the cycle.
While a common implementation of this component consists in imposing a fixed subcooling degree $\Delta T_{sub}$ on

the hot side, so that the fluid enters the expansion valve as subcooled liquid, a different approach is adopted in this work. The IHX is modeled by imposing a pinch-point temperature difference $\Delta T_{rec}$ on the heat exchanger, which links the compressor inlet condition (state 1) to the hot-side outlet (state 3) as follows:

$$T_1 = T_3 - \Delta T_{rec} \tag{2}$$

where state 3 corresponds to the refrigerant leaving the hot side of the IHX as saturated liquid, and state 6 to the refrigerant exiting the evaporator as saturated vapor at a known temperature $T_6$. Since the same working-fluid mass flow rate flows through both sides of the IHX, the shape of the temperature profiles is determined by the difference in specific heat capacity between the liquid and vapor phases. Owing to the higher specific heat capacity of the liquid, the liquid-side temperature profile is less steep than that of the vapor side. As a result, the smallest temperature difference is reached at the hot-side outlet (state 3), which therefore represents the controlling pinch point adopted in the present model.
The energy balance across the heat exchanger then yields:

$$\frac{\dot{Q}_{IHX}}{\dot{m}_{HP}} = h_3 - h_4 = h_1 - h_6 \tag{3}$$

from which the specific enthalpy $h_4$ is directly obtained, allowing the thermodynamic state at the expansion valve inlet (state 4) to be fully determined.
The following modeling assumptions apply to the IHX: the pinch-point temperature difference $\Delta T_{rec}$ is prescribed as an input parameter, and the superheating degree is not imposed directly but is instead obtained as a result of the energy balance in Equation 3.

In addition to the cycle optimization, the recuperator pinch-point temperature difference, $\Delta T_{rec}$, is treated as a design variable. Reducing $\Delta T_{rec}$ increases the amount of internal heat recovery and, consequently, the cycle COP, but requires a larger heat transfer area and therefore higher capital investment. Conversely, larger values of $\Delta T_{rec}$ reduce the required heat exchanger size and investment cost, while lowering the thermodynamic performance of the cycle. The optimal value is obtained through a thermo-economic optimization, whose results are discussed in Section 4.1.2.

### 3.2.3 Two-stage cascade configuration

The two-stage cascade configuration consists of two separate vapor-compression cycles – a low-stage (LS) cycle and a high-stage (HS) cycle – thermally coupled through a cascade heat exchanger. The LS cycle absorbs heat from the geothermal brine at the evaporator and rejects it to the cascade HEX, which in turn acts as the evaporator for the HS cycle; the HS cycle then rejects heat to the district heating network through its condenser.

The intermediate temperature level, which governs the thermal coupling between the two cycles, is defined as a weighted average between the LS evaporation temperature and the HS condensation temperature:

$$T_{switch} = (1 - w_{LS})\, T_{evap,LS} + w_{LS}\, T_{cond,HS} \tag{4}$$

where $w_{LS} \in [0, 1]$ is a weighting factor that redistributes the temperature lift between the two stages. This parameter is optimized in order to identify the intermediate temperature that minimizes the total annuities.
The condensation temperature of the LS cycle and the evaporation temperature of the HS cycle are then derived from $T_{switch}$ by symmetrically applying the cascade heat exchanger temperature difference $\Delta T_{cascade} = 5\,\mathrm{K}$:

$$T_{cond,LS} = T_{switch} + \frac{\Delta T_{cascade}}{2} \tag{5}$$

$$T_{evap,HS} = T_{switch} - \frac{\Delta T_{cascade}}{2} \tag{6}$$

Within the cascade heat exchanger, the LS refrigerant undergoes de-superheating and condensation, rejecting heat to the HS refrigerant, which simultaneously evaporates in counter-current and reaches the superheated vapor state at the HS compressor inlet.
The heat duty of the cascade HEX is therefore:

$$\dot{Q}_{cascade} = \dot{m}_{LS}\, (h_2 - h_3) \tag{7}$$

where state 2 is the LS compressor outlet and state 3 is the saturated liquid exiting the cascade HEX on the LS side. The HS mass flow rate is then obtained from the energy balance on the HS side:

$$\dot{m}_{HS} = \frac{\dot{Q}_{cascade}}{h_5 - h_8} \tag{8}$$

where state 5 is the HS compressor inlet and $h_8$ is the specific enthalpy of the saturated liquid at the HS expansion valve outlet.
The following modeling assumptions apply to this configuration: a superheating degree of $\Delta T_{sh} = 10\,\mathrm{K}$ is imposed at the inlet of both compressors, pressure drops across the cascade heat exchanger are neglected, and subcooling is not applied on either side ($\Delta T_{sub} = 0$).

## 3.3. Economic Model

The economic assessment of the system is carried out by means of a model whose primary evaluation metric is the levelised Cost of Heat (LCOH) of the complete system, comprising the heat pump and the auxiliary boiler. Drawing on the results of the annual thermodynamic simulation, the model determines the electrical energy consumption of the heat pump, the useful heat output it delivers, and the auxiliary thermal contribution required from the boiler. The system LCOH is defined as:

$$LCOH_{sys} = \frac{AN_{HP} + AN_{Boiler}}{Q_{HP} + Q_{Boiler,th}} \tag{9}$$

where $AN_{HP}$ and $AN_{Boiler}$ are the total annuities of the heat pump and the auxiliary boiler, respectively, and the denominator represents the total useful heat delivered to the district heating network.
In addition to the LCOH, the discounted payback time (PBT) is adopted as a complementary economic indicator. Whereas the LCOH expresses the specific cost of the heat delivered, the PBT measures the time required for the cumulative discounted savings generated by the heat pump investment to offset its initial capital cost. The savings in each year are evaluated as the difference in operating cost between the reference case, in which the entire thermal demand is met by the natural gas boiler alone, and the integrated heat-pump-plus-boiler system:

$$\Delta C_{\mathrm{op},k} = C_{\mathrm{op},k}^{\text{boiler-only}} - C_{\mathrm{op},k}^{\text{HP+boiler}} \tag{10}$$

where $C_{\mathrm{op},k}^{\text{boiler-only}}$ is the operating cost of supplying the full annual demand with the boiler alone and $C_{\mathrm{op},k}^{\text{HP+boiler}}$ that of the integrated system, both evaluated in year $k$. The annual cash flows are discounted using the same interest factor $q$ adopted in the annuity method (Appendix C). The discounted payback time is then the number of years after which the cumulative discounted savings equal the additional investment required by the heat pump:

$$\sum_{k=1}^{\mathrm{PBT}} \frac{\Delta C_{\mathrm{op},k}}{q^k} = A_{0,\mathrm{HP}} \tag{11}$$

where $A_{0,\mathrm{HP}}$ is the heat pump investment cost. A shorter payback indicates a more rapidly amortized investment; the metric is particularly informative when comparing scenarios with different energy and carbon prices, as these directly govern the magnitude of the annual savings through Equation 10.
Consistent with the definition of the reference system presented in Section 2.1, the existing geothermal infrastructure is treated as a fixed boundary condition. Therefore, the economic analysis only accounts for the investment costs of the heat pump and the operational costs of the auxiliary boiler. The capital costs associated with the existing boiler, the geothermal wells, the brine extraction pump, and the primary heat exchanger are excluded from the analysis and are therefore not included in $AN_{\mathrm{Boiler}}$.
The capital expenditure (CAPEX) of each component is estimated by means of an exponential scaling correlation [38, 39]:

$$C_i = C_{i,0} \cdot \left(\frac{X}{X_{i,0}}\right)^n \tag{12}$$

where $C_{i,0}$ is the reference cost of the component, $X_{i,0}$ is the corresponding reference scaling parameter, $X$ is the value of the scaling parameter for the sized component, and $n$ is the scaling exponent [10].

Table 2: Cost estimation correlation parameters.

| Component | $C_{i,\mathrm{ref}}$ | $X_{i,\mathrm{ref}}$ | $y$ | Ref. year | Source |
|---|---|---|---|---|---|
| Plate heat exchanger | 15.526 € | $42\,\mathrm{m}^2$ | 0.80 | 2013 | [40] |
| Semi-hermetic screw compressor | 19.850 € | $279.8\,\mathrm{m}^3/\mathrm{h}$ | 0.73 | 2013 | [40] |
| Working fluid receiver | 1.444 € | $0.089\,\mathrm{m}^3$ | 0.63 | 2013 | [40] |
| Gas-fired boiler | 256 € | 1 kW | 0.745 | 1982 | [41] |

This correlation is applied to the main heat pump components, sized at the design point, namely the evaporator, condenser, twin-screw compressor, and working fluid receiver sized on the maximum auxiliary load. The process followed to size the heat exchangers is explained in the appendix B.
The cost of the working fluid is estimated from the refrigerant inventory contained in the heat exchangers and in the liquid receiver. Following the approach proposed by Braimakis and Karellas [36], the receiver volume is assumed to be 1.2 times the total refrigerant-side volume of the heat exchangers:

$$V_{rec} = 1.2 \sum_i V_{HX,i} \tag{13}$$

The total working-fluid cost is then evaluated as

$$C_{fluid} = (m_{wf,HEX} + K\, V_{rec}\, \rho_{wf})\, c_{fluid} \tag{14}$$

where $m_{wf,HEX}$ is the total mass of refrigerant contained in the heat exchangers, $K$ is the receiver filling factor, fixed at 0.8, $V_{rec}$ is the receiver volume, $\rho_{wf}$ is the density of the working fluid at the receiver conditions (i.e. downstream of the condenser), and $c_{fluid}$ is the specific cost of the refrigerant as reported in 1.
Annual costs are computed following the annuity method in accordance with VDI 2067 [42] and described in the appendix C, distinguishing three contributions: the capital-bound annuity $AN_K$, associated with the initial investment; the demand-bound annuity $AN_V$, covering energy consumption costs; and the operation-bound annuity $AN_B$, accounting for maintenance and inspection, calculated as 2.5% of the CAPEX per year. For the heat pump, the dominant contribution to $AN_V$ is the cost of electrical energy, whereas for the auxiliary boiler it is the cost of natural gas.

In order to assess the robustness of the results with respect to market conditions, the model evaluates multiple scenarios of electricity price, natural gas price, and $CO_2$ emission cost.
Since electricity represents the main operating cost of the heat pump, a sensitivity analysis is performed considering three scenarios representative of the German electricity market: an optimistic scenario corresponding to the 2019 average market price of 36.64 €/MWh, a pessimistic scenario corresponding to the peak recorded in 2022 of 230.57 €/MWh, and an intermediate scenario based on the mean value over the period considered, equal to 133.61 €/MWh [43].
The model further considers three natural gas price scenarios representative of the German market:

- 27.8 €/MWh, corresponding to the 2019 market price;
- 47.3 €/MWh, intermediate mean scenario;
- 66.8 €/MWh, corresponding to the 2023 market price [44].

The cost of $CO_2$ emissions is introduced as a direct surcharge on the fuel price, considering two carbon pricing levels: a moderate level, representative of 2020 market conditions, amounting to 16.47 €/ton (3.3 €/$\mathrm{MWh_{th}}$), and a high level, projected for the coming years, amounting to 116.7 €/ton (23.4 €/$\mathrm{MWh_{th}}$) [45, 46].

# 4. Results

This chapter presents and discusses the thermodynamic and economic results obtained for the configurations under analysis. The discussion is structured in two stages: first, the thermodynamic results are presented for each configuration with reference to the most promising working fluid identified through the screening procedure; subsequently, a complete techno-economic analysis is carried out for the globally most favourable scenario, selected on the basis of the thermodynamic performance and the preliminary cost indicators described in the following section.

## 4.1. Thermodynamic results

### 4.1.1 Single-stage results

The analysis of the single-stage configuration begins with the determination of the compressor size required to cover the peak thermal demand of the DHN, following the procedure outlined in Section 3.1, this procedure is repeated for each working fluid under consideration. As an illustrative example, Figure 7 shows the auxiliary boiler heat contribution as a function of the compressor swept volume for butane (R600): the minimum $V_s$ ensuring complete peak demand coverage is 0.0378 m$^3$.

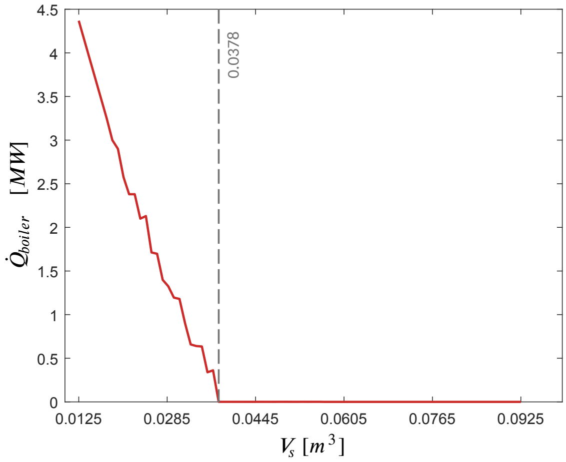


Figure 7: Boiler duty needed for peak load coverage at the maximum DHN operating point with different swept compressor volumes.

The most relevant thermodynamic and economic parameters at the design point are reported in Table 3 for all working fluids analyzed. For each fluid, the table lists the two optimization variables, namely the working fluid mass flow rate $\dot{m}_{HP}$ and the evaporation pressure $p_{evap}$, together with the resulting swept volume $V_s$, the compressor and evaporator thermal powers, and the design-point COP. A preliminary economic assessment is also included, reporting CAPEX, the total annuity AN and the LCOH. The most promising working fluid for this configuration is butane (R600), which exhibits the best trade-off between COP and annuity, yielding the lowest LCOH among all fluids considered. Conversely, R1233zd(E), despite having the highest COP, also presents the highest capital costs that translate into a higher LCOH.

Table 3: Comparison of refrigerants in SS at nominal point.

| Refrigerant | $\dot{m}_{\mathrm{HP}}$ [kg/s] | $p_{\mathrm{evap}}$ [bar] | $V_{\mathrm{s}}$ [m$^3$] | $P_{\mathrm{compr}}$ [MW] | $\dot{Q}_{\mathrm{evap}}$ [MW] | COP [-] | CAPEX [k€/y] | AN [k€/y] | LCOH [€/MWh] |
|---|---|---|---|---|---|---|---|---|---|
| R1234ze(Z) | 41.21 | 2.92 | 0.0429 | 1.56 | 5.5 | 4.3 | 123 | 304 | 95.2 |
| R1233zd (E) | 43.45 | 2.19 | 0.055 | 1.51 | 5.43 | 4.35 | 154 | 351 | 109.7 |
| R600 | 24.42 | 3.82 | 0.0378 | 1.59 | 5.58 | 4.22 | 101 | 273 | 85.9 |
| R600a | 28.86 | 5.37 | 0.0307 | 1.69 | 5.44 | 4 | 99 | 275 | 86.9 |
| R290 | 34.45 | 14.24 | 0.0166 | 2.1 | 5.02 | 3.21 | 69 | 310 | 96.7 |

* *R1234yf results are not available because of the low critical temperature.*

Figures 8 and 9 show the $T$–$s$ and $T$–$Q$ diagrams of the single-stage configuration with butane at peak load and minimum load conditions, respectively. The comparison between the two operating regimes highlights how the simultaneous optimization of the refrigerant mass flow rate and evaporation pressure enables the cycle to adapt effectively to varying thermal demands. At peak load, the higher evaporation pressure reduces the temperature lift, resulting in a COP of 4.23. At minimum load, the reduced mass flow rate and lower evaporation pressure increase the temperature lift, leading to a lower cycle efficiency with a COP of 2.57. This behaviour is consistent with the pinch-point constraints imposed on the heat exchangers and the operational limits of the compressor. Furthermore, the $T$–$Q$ diagrams highlight a markedly different behaviour of the brine-side heat exchange between the two operating conditions: at peak load, the brine undergoes a substantial temperature drop across the evaporator, whereas at minimum load the thermal exchange with the source is considerably more limited, reflecting the much lower heat duty of the cycle.

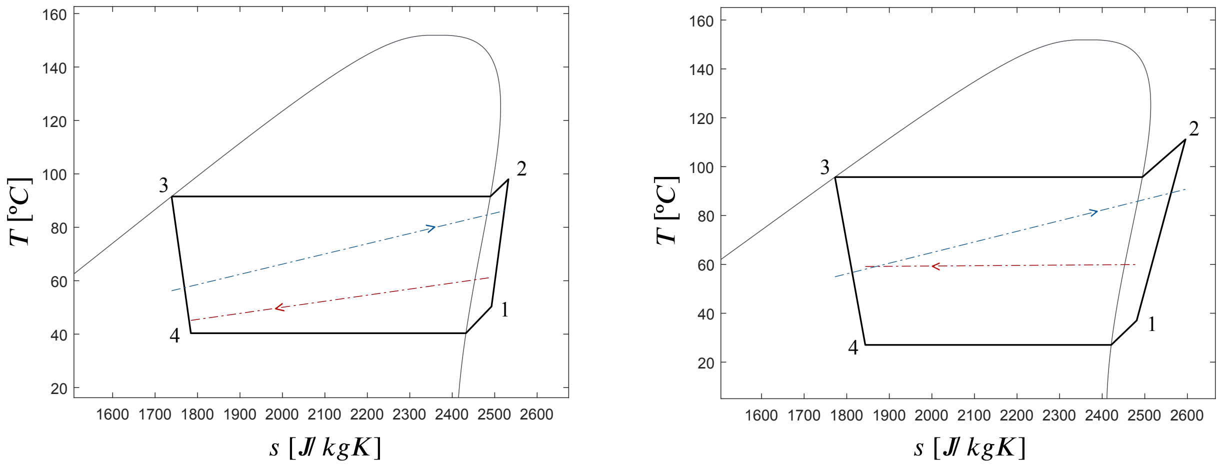


Figure 8: TS diagram of Butane in the SS cycle under peak load and minimum load demand.

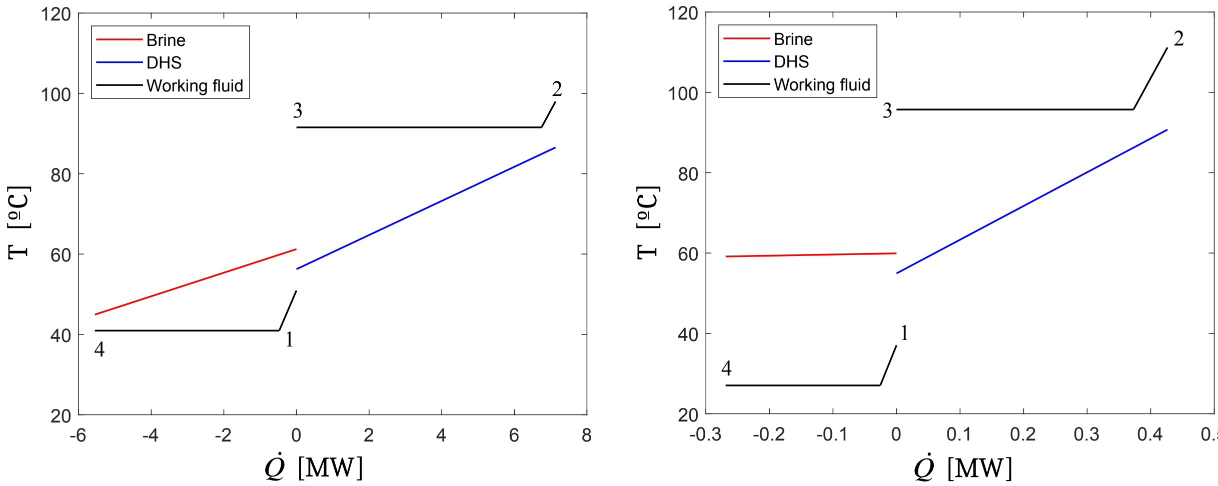


Figure 9: TQ diagram of butane in the SS cycle under peak load and minimum load demand.

Figure 10 reports, respectively, the coefficient of performance and the compressor isentropic efficiency obtained for butane (R600) across the representative typical days into which the annual load profile is aggregated, plotted against the condenser thermal duty $\dot{Q}_{cond}$ and coloured by the corresponding temperature lift $\Delta T_{lift}$. Each point therefore corresponds to a distinct operating condition encountered by the cycle over the year, and the resulting scatter reflects the variability of the annual operation rather than a parametric sweep at fixed boundary conditions.

The COP, shown in Figure 10a, ranges between approximately 4.1 and 5.5 and is governed primarily by the temperature lift. The points are clearly stratified by colour: operating conditions characterized by a low lift (magenta) cluster in the upper part of the plot, reaching the highest COP values, whereas conditions with a high lift (yellow) lie systematically lower. This behaviour is consistent with the thermodynamics of the vapour-compression cycle, in which a smaller temperature difference between the heat sink and the heat source reduces the compression work required per unit of heat delivered, thereby increasing the COP. The dependence on the condenser duty is comparatively weaker and largely mediated by the lift itself, since the most favourable low-lift conditions tend to occur at intermediate-to-high thermal duties.

The isentropic efficiency, shown in Figure 10b, exhibits a markedly different behaviour, following an inverted-U trend as a function of the condenser duty. Starting from values around 76.5 % at the lowest duties, $\eta_{is}$ increases with $\dot{Q}_{cond}$, reaches a maximum of approximately 78.6 % in the intermediate range (about 5 MW to 6 MW), and then decreases again towards the highest duties. This trend is a direct consequence of the part-load behaviour of the twin-screw compressor: at low thermal duty the machine operates far from its design volumetric flow rate, with a corresponding efficiency penalty, while at the highest duties the deviation of the applied pressure ratio from the built-in volume ratio similarly reduces the efficiency. The maximum efficiency is therefore attained at intermediate operating conditions, where the compressor works closest to its nominal point. The few outliers visible below the main trend correspond to type days in which the combination of duty and lift drives the

compressor towards a less favourable operating region.
Overall, the two figures highlight that the off-design performance of the single-stage configuration is the result of two distinct mechanisms: a thermodynamic dependence of the COP on the temperature lift, and a compressor-related dependence of the isentropic efficiency on the thermal duty. The simultaneous optimization of the refrigerant mass flow rate and evaporation pressure described in 3.1 enables the cycle to operate as close as possible to its most efficient region across the full range of annual conditions.

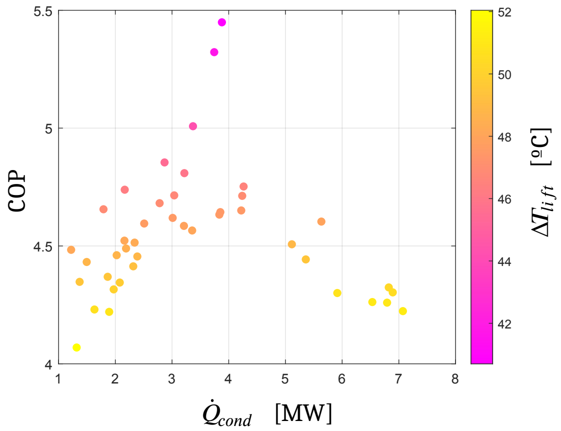


(a) Coefficient of performance.

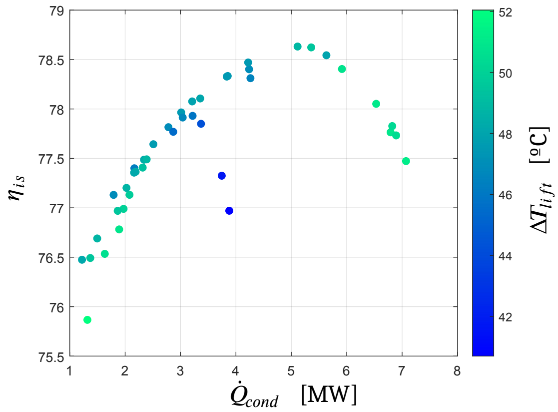


(b) Isentropic efficiency.

Figure 10: COP (a) and compressor isentropic efficiency (b) of butane in the SS annual simulation plotted against the condenser thermal duty and coloured by the temperature lift.

To condense the annual behaviour into a single representative figure, the Seasonal Performance Factor (SPF) is introduced, defined as the ratio between the total useful heat delivered by the heat pump over the year and the total electrical energy absorbed by the compressor over the same period:

$$\mathrm{SPF} = \frac{\sum_i \dot{Q}_{\mathrm{cond},i}\, t_i}{\sum_i P_{\mathrm{el},i}\, t_i} \tag{15}$$

where $\dot{Q}_{\mathrm{cond},i}$ is the condenser thermal duty, $P_{\mathrm{el},i}$ the electrical power absorbed by the compressor, and $t_i$ the duration of the $i$-th operating condition. Unlike the design-point COP, which refers to a single operating condition, the SPF aggregates all annual operating points weighted by their actual duration, and is therefore closely related to the weighted COP of Equation 16, the two metrics being conceptually equivalent and numerically very close. Evaluated at full size ($f_{HP} = 1$), the single-stage configuration with butane attains an SPF of 4.41, higher than the design-point COP of 4.22, reflecting the fact that most annual hours operate at a lower temperature lift, and thus a higher efficiency, than the peak design condition.

### 4.1.2 Single-stage with IHX results

The most relevant thermodynamic and economic parameters obtained at the design point for the single-stage configuration with internal heat exchanger are reported in Table 4. In addition to the optimization variables already considered for the reference configuration, the optimal recuperator temperature difference $\Delta T_{rec}^{opt}$ is also reported, introduced as an additional design parameter.

Table 4: Comparison of refrigerants in SS + IHX at design point.

| Refrigerant | $\dot{m}_{\mathrm{HP}}$ [kg/s] | $p_{\mathrm{evap}}$ [bar] | $V_{\mathrm{s}}$ [$\mathrm{m}^3$] | $\Delta T_{\mathrm{rec}}^{\mathrm{opt}}$ [K] | $P_{\mathrm{compr}}$ [MW] | $\dot{Q}_{\mathrm{evap}}$ [MW] | COP [-] | CAPEX [k€/y] | AN [k€/y] | LCOH [€/MWh] |
|---|---|---|---|---|---|---|---|---|---|---|
| R1234ze(Z) | 34.2 | 2.9 | 0.041 | 9 | 1.5 | 5.63 | 4.5 | 70 | 284 | 88.3 |
| R1233zd (E) | 37.6 | 2.14 | 0.0595 | 13 | 1.48 | 5.64 | 4.55 | 93 | 345 | 103.5 |
| R600 | 20.13 | 3.7 | 0.0382 | 13 | 1.5 | 5.6 | 4.53 | 58 | 256 | 79.1 |
| R600a | 21.9 | 5.3 | 0.028 | 11 | 1.52 | 5.61 | 4.45 | 54 | 248 | 77.5 |
| R290 | 24.3 | 14 | 0.0164 | 7 | 1.84 | 5.3 | 3.67 | 39 | 258 | 79.6 |

* *R1234yf results are not available because of the low critical temperature.*

The introduction of the IHX leads to a generalized improvement of the cycle thermodynamic performance compared to the single-stage configuration. For all refrigerants considered, an increase in COP is observed, accompanied by a reduction in the compressor power absorbed and in the refrigerant mass flow rate required to meet the thermal load. This behaviour is attributable to the recuperative action of the internal heat exchanger, which simultaneously subcools the liquid entering the expansion valve and superheats the vapor drawn into the compressor.

As already observed for the single-stage configuration, hydrocarbons remain the most promising fluids. However, the introduction of the IHX slightly alters the economic performance ranking. While butane (R600) was found to be the most cost-effective refrigerant in the reference case, in the configuration with internal heat exchanger isobutane (R600a) exhibits the lowest LCOH, equal to 77.5 €/MWh, closely followed by butane (R600) at 79.1 €/MWh. The difference between the two fluids remains below 2%, suggesting that they can be regarded as essentially equivalent from an economic standpoint.
The benefit introduced by the IHX varies considerably across the working fluids considered. Butane (R600) shows the most evident improvement among the hydrocarbons, with the COP increasing from 4.22 to 4.53 (+7%). R290 exhibits the largest relative gain, with a COP increase exceeding 14%, while R1233zd(E) shows a more limited improvement of approximately 5%, reaching a COP of 4.55; despite this competitive value, its higher capital cost continues to translate into a higher annuity and, consequently, a higher LCOH. R1234ze(Z) similarly reaches a COP of 4.50, again outperforming the single-stage configuration, but remains penalized on the economic side for the same reason. This variation suggests that the effectiveness of the internal heat exchanger is closely related to the thermophysical properties of the working fluid, and that the achievable benefit cannot be considered uniform across different refrigerants.

In order to further characterize the behaviour of the SS+IHX configuration with the selected fluid, Figures 11 and 12 show the $T$–$s$ and $T$–$Q$ diagrams of isobutane at peak load and minimum load conditions, respectively. Compared to the single-stage configuration, the presence of the recuperator modifies the shape of the cycle by introducing two additional transformations: the superheating of the vapor leaving the evaporator, between states 6 and 1, and the subcooling of the liquid leaving the condenser, between states 3 and 4. This allows the useful enthalpy difference at the evaporator to be increased, thereby reducing the refrigerant mass flow rate required to deliver the same thermal output to the DHN.
At peak load, the cycle exhibits extensive thermal interaction on both the source and the load side: the $T$–$Q$ diagram shows a substantial temperature drop of the brine and a complete heating of the DHN fluid up to the required temperature. At minimum load, by contrast, the exchanged power is considerably lower and the contribution of the geothermal source is limited, as shown by the shorter extent of the brine curve in the $T$–$Q$ diagram. In both cases, the recuperator nonetheless maintains a consistent thermal separation between the temperature levels of the cycle, ensuring compliance with the pinch-point constraints imposed on the heat exchangers.

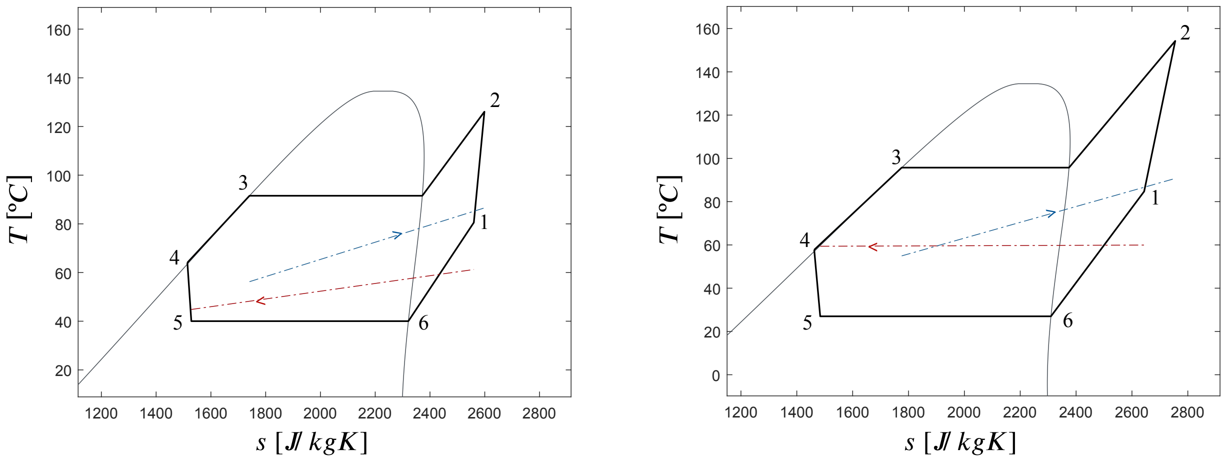


Figure 11: TS diagram of Isobutane in the SS+IHX cycle under peak load and minimum load demand.

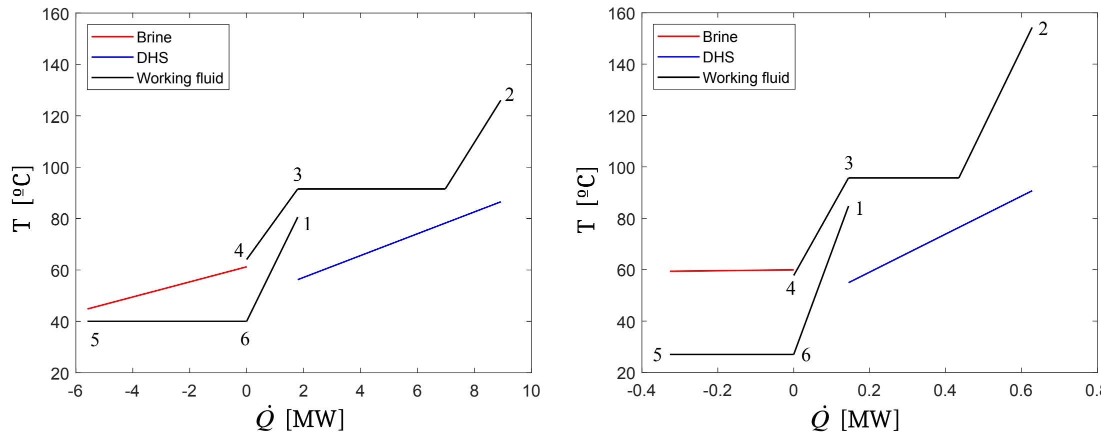


Figure 12: TQ diagram of Isobutane in the SS+IHX cycle under peak load and minimum load demand.

Figure 13 reports the design-point coefficient of performance and the compressor isentropic efficiency obtained for isobutane (R600a) in the SS+IHX configuration across the representative typedays, plotted against the condenser thermal duty $\dot{Q}_{cond}$ and coloured by the corresponding temperature lift $\Delta T_{lift}$. As for the single-stage case, each point corresponds to a distinct operating condition encountered over the year, so that the scatter reflects the variability of the annual operation.

The COP, shown in Figure 13a, ranges between approximately 4.4 and 5.6 and is again governed primarily by the temperature lift, with a clear stratification of the points by colour: low-lift conditions (magenta) attain the highest COP values, while high-lift conditions (yellow) lie systematically lower. With respect to the single-stage configuration, the entire point cloud is shifted upward, reflecting the recuperative action of the internal heat exchanger, which simultaneously subcools the liquid entering the expansion valve and superheats the vapour drawn into the compressor, thereby reducing the specific compression work and increasing the COP across the full range of annual conditions. The dependence on the condenser duty is more pronounced than for the reference cycle, with the COP decreasing almost monotonically as $\dot{Q}_{cond}$ increases; this reflects the fact that, in the annual operation, the highest thermal duties coincide with the highest temperature lifts, which dominate the cycle efficiency.

The isentropic efficiency, shown in Figure 13b, follows the same inverted-U trend already observed for the single-stage configuration, since it is governed by the part-load behaviour of the twin-screw compressor and is therefore largely independent of the cycle architecture. Starting from values around 75 % at the lowest duties, $\eta_{is}$ increases with $\dot{Q}_{cond}$, reaching a plateau of approximately 78.5 % in the intermediate-to-high range (about 5 MW to 6 MW), before decreasing slightly towards the highest duties. As discussed for the reference cycle, this behaviour arises because the compressor operates closest to its nominal point at intermediate duties, whereas at low duty the machine works far from its design volumetric flow rate and at the highest duties the applied pressure ratio deviates from the built-in volume ratio, both conditions entailing an efficiency penalty.

Overall, the comparison with the single-stage configuration confirms that the introduction of the internal heat exchanger improves the coefficient of performance over the entire range of annual operating conditions, while leaving the compressor isentropic efficiency essentially unchanged, as the latter depends on the machine operating point rather than on the presence of the recuperator.

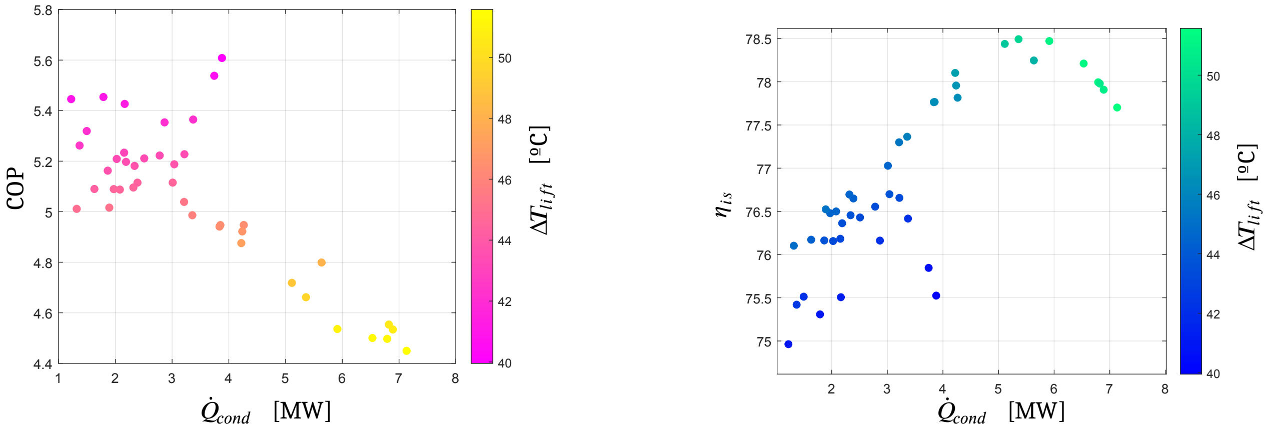


(a) Coefficient of performance.

(b) Isentropic efficiency.

Figure 13: COP (a) and compressor isentropic efficiency (b) of isobutane in the SS+IHX annual simulation plotted against the condenser thermal duty and coloured by the temperature lift.

Consistently with the upward shift of the COP cloud discussed above, the single-stage cycle with internal heat exchanger attains a Seasonal Performance Factor of 4.74 (at $f_{HP} = 1$), the highest among the three configurations. This represents an improvement of approximately 7.5 % over the single-stage baseline (SPF = 4.41) and confirms, on an annual-energy basis, the benefit of the recuperative action already observed at the design point.

**Optimization of the pinch-point at the recuperator.** The selection of the optimal value of $\Delta T_{rec}$ was carried out by analyzing the behaviour of several performance and economic indicators as a function of the recuperator temperature difference, reported in Figures 14a, 14b, 15a, and 15b. The results show that the design COP tends to decrease as $\Delta T_{rec}$ increases, while the weighted COP exhibits the same decreasing trend, indicating that high values of $\Delta T_{rec}$ penalize the average annual performance of the cycle.
The weighted COP is defined as:

$$COP_w = \frac{\sum_i Q_{DHS,i} \cdot COP_i \cdot h_i}{\sum_i Q_{DHS,i} \cdot h_i} \tag{16}$$

Conversely, the annuity and the LCOH exhibit a minimum-seeking trend: for excessively low values of $\Delta T_{rec}$, the benefit of internal recovery is not yet fully exploited, whereas for excessively high values the deterioration of thermodynamic performance results in increased operating costs. In each figure, the highlighted point corresponds to the economically optimal value of $\Delta T_{rec}$.
The value $\Delta T_{rec} = 11$ K therefore represents the best compromise for isobutane. At this value, the minimum LCOH is observed together with the lowest annuity, amounting to approximately 248 k€/y. Although the design COP is slightly higher for lower values of $\Delta T_{rec}$, the final selection is not based exclusively on the nominal-point performance, but on the overall trade-off between annual efficiency, annual cost, and levelised cost of heat.

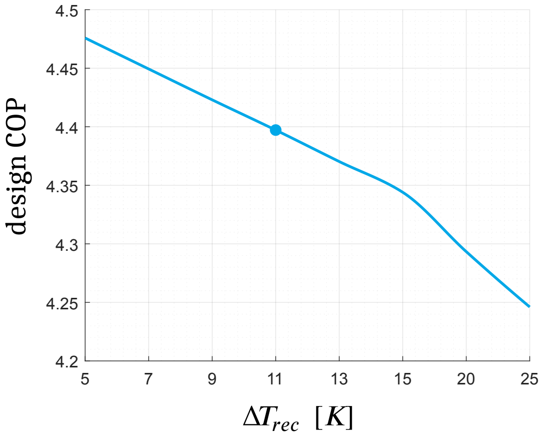


(a) Design-point COP.

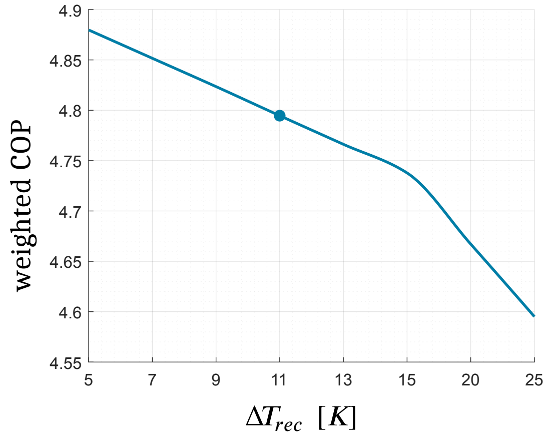


(b) Weighted annual COP.

Figure 14: a) Design-point COP and b) weighted annual COP as a function of the recuperator temperature difference for Isobutane in the SS+IHX configuration.

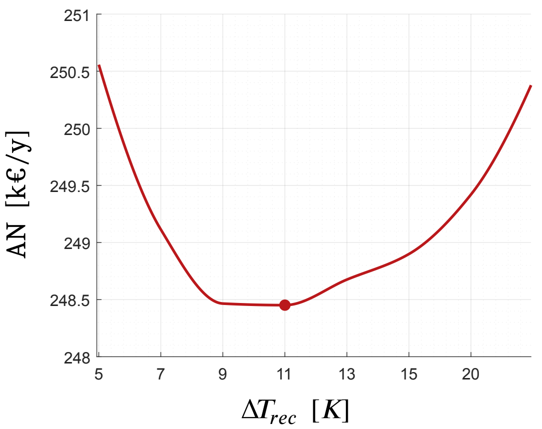


(a) Total annuity AN.

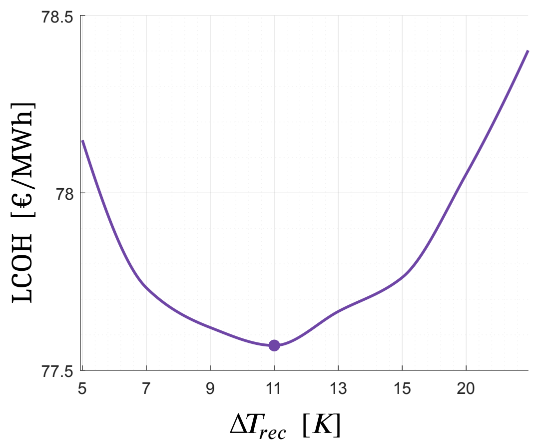


(b) Levelised cost of heat.

Figure 15: a) Total annuity AN and b) LCOH as a function of the recuperator temperature difference for Isobutane in the SS+IHX configuration.

### 4.1.3 Two-stage cascade results

The thermodynamic and economic parameters obtained at the design point for the two-stage cascade configuration are reported in Table 5 for all the fluid combinations investigated. In addition to the single-fluid cases, the table includes the physically motivated pairings described in Section 2.2, in which the low-critical-temperature fluids (R290 and R1234yf) are assigned to the low-stage (LS) circuit and the higher-critical-temperature fluids to the high-stage (HS) circuit. For each combination, the table lists the LS mass flow rate, the LS evaporation pressure, the swept volumes of the two compressors, the total compressor power, the evaporator and condenser thermal duties, the design-point COP, and the preliminary economic indicators.

Table 5: Comparison of refrigerants in Cascade at design point.

| WF LS | WF HS | $\dot{m}_{\mathrm{HP,LS}}$ [kg/s] | $p_{\mathrm{eva,LS}}$ [bar] | $V_{\mathrm{s,LS}}$ [m$^3$] | $V_{\mathrm{s,HS}}$ [m$^3$] | $P_{\mathrm{comp,tot}}$ [MW] | $\dot{Q}_{\mathrm{eva}}$ [MW] | COP [-] | CAPEX [k€/y] | AN [k€/y] | LCOH [€/MWh] |
|---|---|---|---|---|---|---|---|---|---|---|---|
| R1234yf | R1233zde | 55.3 | 10.3 | 0.0142 | 0.0290 | 1.65 | 5.5 | 4.1 | 240 | 492 | 155.4 |
| R290 | R1233zde | 22.8 | 13.8 | 0.0113 | 0.0290 | 1.64 | 5.49 | 4.13 | 193 | 419 | 132.2 |
| R1234yf | R600 | 55 | 10.3 | 0.0142 | 0.0210 | 1.67 | 5.47 | 4 | 181 | 404 | 126.9 |
| R290 | R600 | 22.8 | 13.8 | 0.0113 | 0.0214 | 1.66 | 5.47 | 4.1 | 140 | 340 | 107.1 |
| R1234yf | R1234ze(Z) | 55.1 | 10.3 | 0.0142 | 0.0229 | 1.66 | 5.47 | 4.1 | 199 | 430 | 135.7 |
| R290 | R1234ze(Z) | 22.8 | 13.8 | 0.0112 | 0.0229 | 1.65 | 5.48 | 4.1 | 157 | 366 | 114.9 |
| R1234yf | R600a | 54.8 | 10.3 | 0.0142 | 0.0172 | 1.7 | 5.44 | 4 | 178 | 403 | 126.6 |
| R290 | R600a | 22.6 | 13.8 | 0.0113 | 0.0172 | 1.7 | 5.45 | 4 | 136 | 343 | 107.3 |

Among all the combinations considered, the propane/butane pairing (R290 in the LS circuit and R600 in the HS circuit) exhibits the best economic performance, yielding the lowest LCOH of 107.1 €/MWh together with the lowest total annuity of 340 k€/y. The isobutane-based pairing (R290/R600a) is essentially equivalent, with an LCOH of 107.3 €/MWh, while all the remaining combinations, and in particular those employing R1233zd(E) or R1234ze(Z) in the high stage, are penalized by higher capital costs that translate into a higher annuity and levelised cost of heat. It is worth noting that, even for the most favourable pairing, the cascade configuration attains an LCOH substantially higher than that of the single-stage cycle with internal heat exchanger discussed in Section 4.1.2. This is a direct consequence of the moderate temperature lift characterizing the present application: the thermodynamic advantage of two-stage compression, which becomes significant only for large temperature lifts, does not compensate for the additional investment associated with the second compressor and the cascade heat exchanger.The present results are therefore in line with the conclusions reported in the literature, where cascade configurations are generally recommended for applications requiring high temperature lifts, while single-stage solutions remain more attractive for moderate operating conditions [14]. The propane/butane pairing is therefore adopted as the reference case for the subsequent analysis of this configuration.
Figures 16 and 17 show, respectively, the T–s and T–Q diagrams of the propane/butane cascade at peak load and minimum load conditions. The T–s diagram clearly displays the two thermally coupled loops: the low-stage cycle, which absorbs heat from the geothermal brine at the evaporator, and the high-stage cycle, which rejects heat to the district heating network at the condenser, the two circuits being linked through the cascade heat exchanger at the intermediate temperature level. The T–Q diagram highlights the heat transfer chain across the components: at peak load, the brine undergoes a substantial temperature drop across the LS evaporator and the DHN fluid is heated up to the required supply temperature by the HS condenser, while the cascade heat exchanger ensures the thermal coupling between the two stages. At minimum load, by contrast, the exchanged power is considerably lower and the contribution of the geothermal source is correspondingly reduced, as reflected in the shorter extent of the brine curve. In both operating regimes, the pinch-point constraints imposed on all heat exchangers are satisfied.

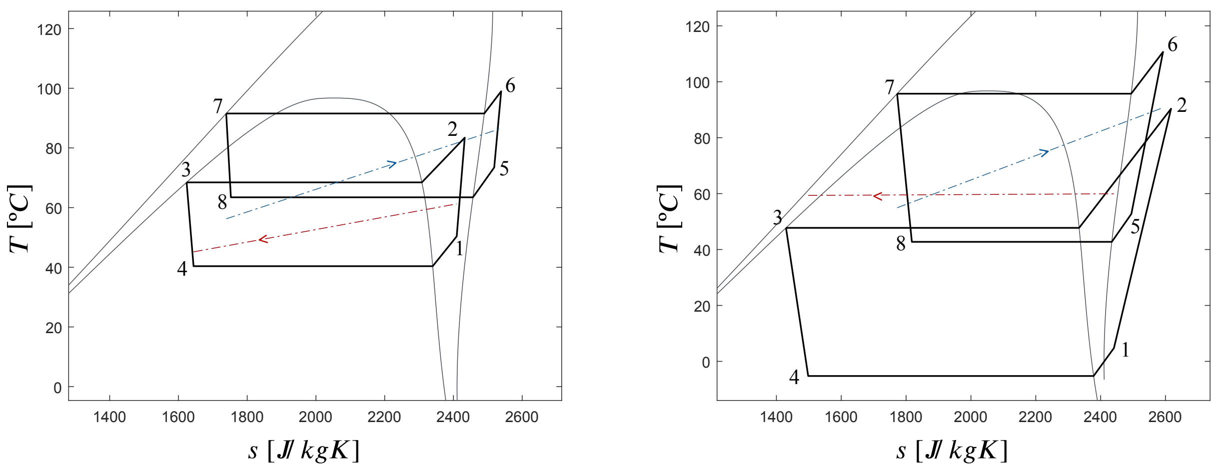


Figure 16: T–s diagram of the propane/butane cascade cycle under peak load and minimum load demand.

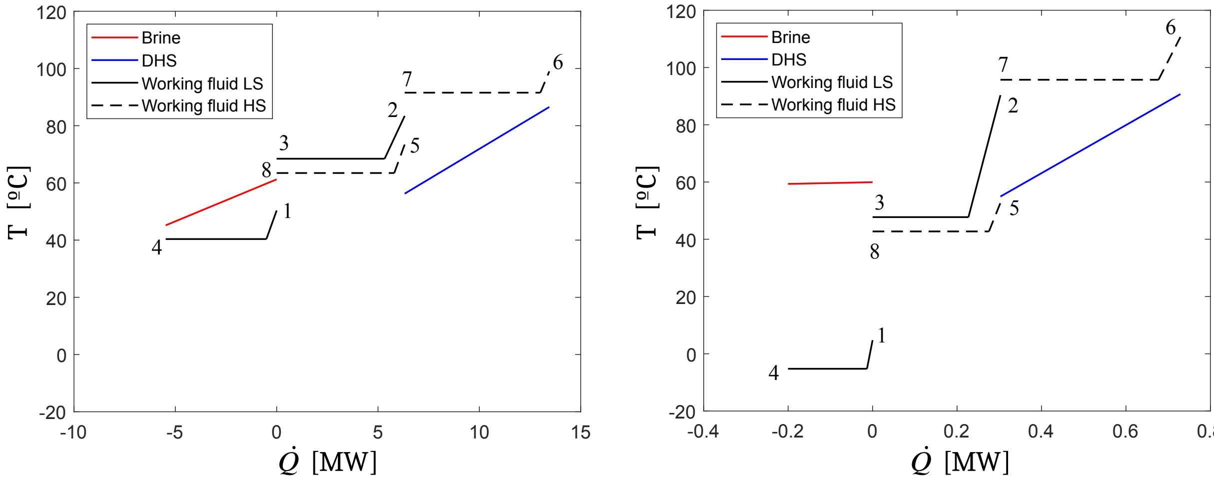


Figure 17: T–Q diagram of the propane/butane cascade cycle under peak load and minimum load demand.

Figure 18 reports the coefficient of performance (a) and the compressor isentropic efficiencies of the low-stage (b) and high-stage (c) circuits for the propane/butane cascade across the representative typedays, plotted against the condenser thermal duty and coloured by the temperature lift. As for the single-stage and SS+IHX cases, each point corresponds to a distinct annual operating condition rather than to a parametric sweep. The COP, shown in Figure 18a, ranges between approximately 4.0 and 4.8 and is again governed primarily by the temperature lift, with low-lift conditions (magenta) clustering at the top of the plot and high-lift conditions (yellow) lying systematically lower; the overall values are lower than those of the single-stage and SS+IHX configurations, consistent with the additional irreversibilities introduced by the cascade heat exchanger and the second compression stage. The two isentropic-efficiency plots follow the same inverted-U trend already observed for the single-stage machines, since both compressors are described by the same twin-screw model: efficiency increases from the lowest duties, reaches a plateau in the intermediate range, and decreases slightly at the highest duties. The low-stage and high-stage compressors exhibit comparable efficiency levels across most of the annual operation, indicating that, at the optimal weighting factor, the overall temperature lift is well balanced between the two stages so that neither compressor is driven far from its design pressure ratio, an aspect examined in detail in the following paragraph.

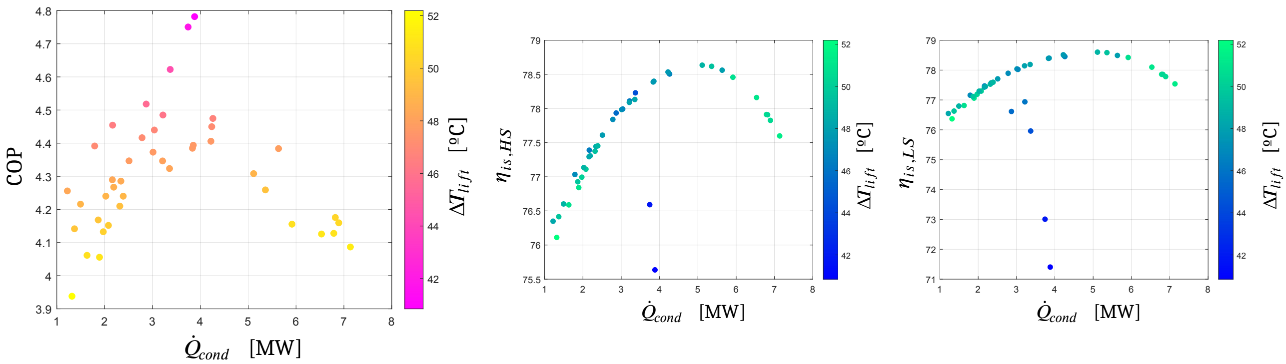


Figure 18: COP (a) and compressor isentropic efficiencies of the low-stage (b) and high-stage (c) circuits for the propane/butane cascade in the annual simulation, plotted against the condenser thermal duty and coloured by the temperature lift.

On an annual basis, the propane/butane cascade attains a Seasonal Performance Factor of 4.11, the lowest of the three configurations. This is consistent with the thermodynamic penalty of the two-compressor architecture at the moderate temperature lift of the present application, and mirrors the LCOH ranking, in which the cascade proves the least competitive solution.

**Optimization of the intermediate temperature level.** As introduced in Section 3.2.3, the intermediate temperature level governing the thermal coupling between the two stages is defined through the weighting

factor $w_{LS}$, which redistributes the overall temperature lift between the low- and high-stage circuits (Equation 4). The value of $w_{LS}$ was optimized in order to minimize the system cost. The analysis was restricted to the range $w_{LS} \in [0.4, 0.7]$: outside this interval, the resulting operating conditions were found to be unfeasible, leading either to supercritical operation of the high-stage cycle or to non-physical low-stage cycles with negative COP, and were therefore excluded.
Figures 20b, 20a, and 19 report, respectively, the system LCOH, the breakdown of the heat pump annuity, and the mean total compressor electric power as a function of $w_{LS}$. All three indicators exhibit a minimum-seeking behaviour, with the optimum located at $w_{LS} = 0.5$. Since the annual heat delivered to the network (the denominator of the LCOH) is essentially independent of $w_{LS}$, the levelised cost of heat follows directly the behaviour of the total annuity: any variation in the annuity, or in one of its components, is reflected in a proportional variation of the LCOH.

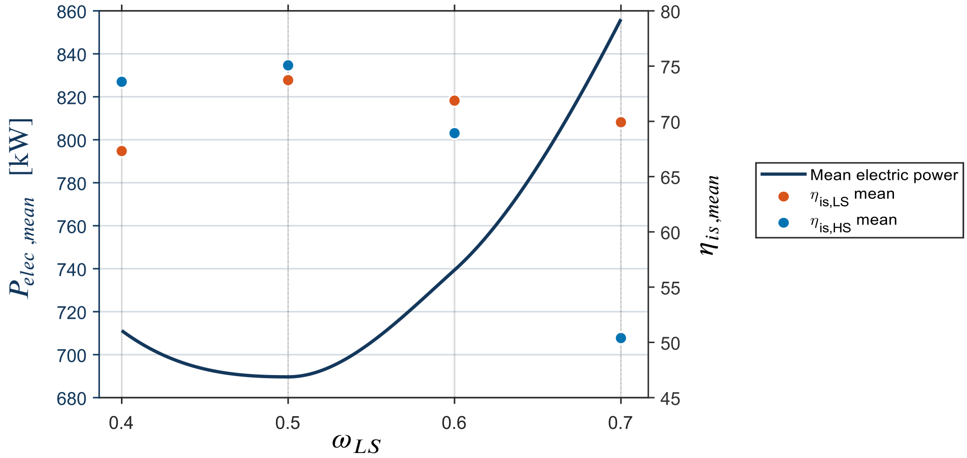


Figure 19: Mean total compressor electric power and mean isentropic efficiencies of the LS and HS compressors as a function of the weighting factor for the propane/butane cascade configuration.

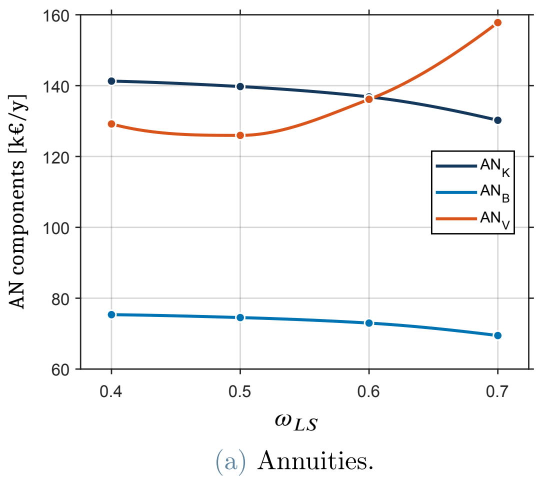


(a) Annuities.

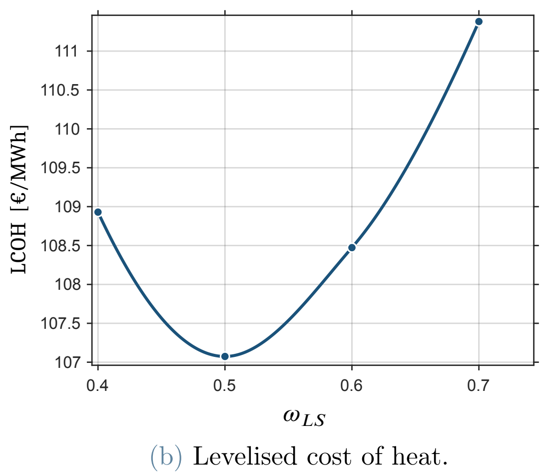


(b) Levelised cost of heat.

Figure 20: a) Breakdown of the heat pump annuity and b) system LCOH as a function of the weighting factor for the propane/butane cascade configuration.

The breakdown of the annuity in Figure 20a shows that the capital-bound annuity $AN_K$ and the operation-bound annuity $AN_B$ vary only marginally with $w_{LS}$, whereas the demand-bound annuity $AN_V$, associated with the electricity consumption of the compressors, is the dominant driver of the trend: it reaches its minimum in $w_{LS} = 0.5$ and increases markedly as $w_{LS}$ departs from this value. The LCOH and the annuity therefore mirror the behaviour of the compressor electrical consumption.
This behaviour is explained by the dependence of $P_{elec}$ on the isentropic efficiency of the two compressors. Figure 19 shows that the mean total electric power is minimized at $w_{LS} = 0.5$, increasing from approximately 690 kW at the optimum to about 856 kW at $w_{LS} = 0.7$. As the weighting factor departs from the value that balances the temperature lift between the two stages, one of the two compressors is pushed far from its design

pressure ratio, which collapses its isentropic efficiency on a significant number of typedays and consequently lowers the annual-mean isentropic efficiency. This is illustrated in Figure 19, which presents the mean isentropic efficiencies of the LS and HS compressors for $w_{LS} = 0.5$ and $w_{LS} = 0.7$: at the optimum, the mean efficiencies of the two stages are both high and close to each other, whereas at $w_{LS} = 0.7$ they decrease and split apart, the reduced mean efficiency directly increases the electrical power absorbed to deliver the same thermal output, and hence the demand-bound annuity and the LCOH.
It should be noted that, for the cascade configuration, the built-in volume ratio adopted in the compressor model differs from the value used for the single-stage cycles. Since the overall pressure ratio is shared between the two compressors arranged in series a per-stage value equal to the square root of the reference figure, $\sqrt{3.1} \approx 1.76$, was adopted for both compressors, consistently with the splitting of the compression between the two stages.
On the basis of this analysis, the value $w_{LS} = 0.5$ was adopted for all the simulations of the cascade configuration presented in this work.

## 4.2. Techno-economic results for selected scenarios

The thermo-economic sizing analysis was carried out for all the investigated heat pump configurations. However, only the results corresponding to the most promising solution are presented in detail. Based on the thermodynamic results discussed in Section 4.1, the configuration exhibiting the lowest LCOH is the single-stage cycle with internal heat exchanger (SS+IHX) operating with isobutane. As outlined in the methodology (Figure 5), the installed heat pump capacity is progressively reduced, with the residual thermal demand supplied by an auxiliary natural gas boiler.

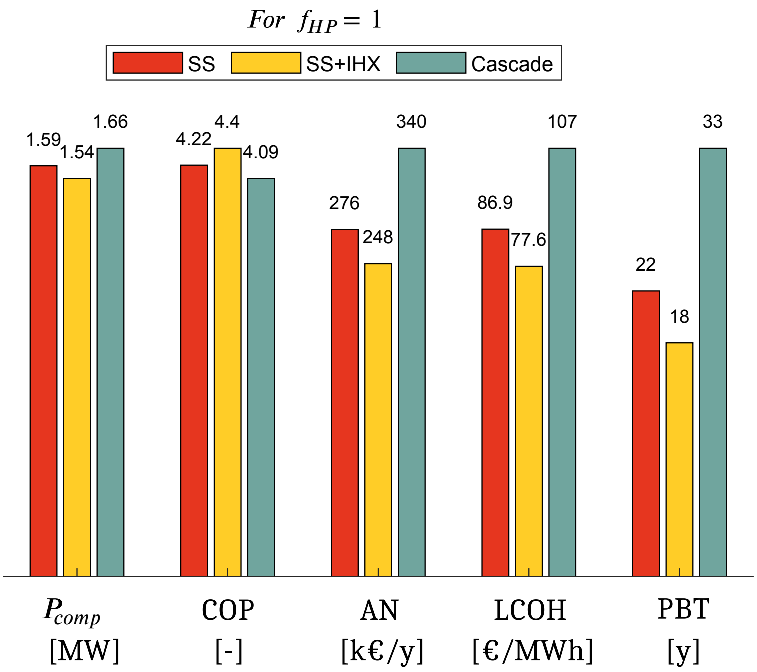


Figure 21: Comparison of the three cycle configurations (SS, SS+IHX, cascade) across the main thermodynamic and economic indicators at the design point: compressor power, COP, total annuity, LCOH, and discounted payback time.

The selection of the SS+IHX configuration with isobutane is summarized in Figure 21, which compares the three cycle architectures across the most relevant thermodynamic and economic indicators at the design point. While the three configurations achieve comparable electric power and coefficient of performance, the SS+IHX cycle attains the lowest total annuity (AN) and, consequently, the lowest levelised cost of heat, equal to 77.6 €/MWh against 86.9 €/MWh for the single-stage cycle and 107 €/MWh for the cascade configuration. The cascade arrangement, despite the additional design flexibility offered by the two-fluid pairing, is penalized by the higher component count and the larger total investment, which outweigh its thermodynamic benefits at the moderate temperature lift characterizing this application. The same ranking is reflected in the discounted payback time reported in the last group of bars: the SS+IHX cycle amortizes the heat pump investment in approximately 18 years, the shortest of the three, against 22 years for the single-stage cycle and 33 years for the cascade. The fact that the SS+IHX configuration simultaneously attains the lowest LCOH and the shortest payback confirms the consistency of the two economic indicators and reinforces the selection of this configuration. It should be noted that these payback values refer to the baseline energy-price scenario, without $CO_2$ emission cost; as shown in Section 4.2.1, the introduction of carbon pricing shortens the payback substantially by increasing the value of the natural gas displaced by the heat pump. The single-stage configuration with internal heat exchanger therefore represents the most favourable compromise between cycle efficiency and capital expenditure, and is adopted as the reference scenario for the sizing study presented hereafter.

Figure 22 reports the breakdown of the annualized system costs as a function of the HP sizing factor, distinguishing between the annualized CAPEX of the heat pump, its OPEX, and the OPEX associated with the auxiliary boiler. As the installed heat pump sizing factor increases, its annualized investment cost and operating cost both rise, the former reflecting the larger sizing of the main components, the latter the growing share of the annual thermal demand met by the vapor-compression cycle rather than by the boiler. The heat pump operating cost is primarily driven by the electrical consumption of the compressor and scales with the annual electricity absorbed and the electricity price assumed in the base case, equal to 133.6 €/MWh. Conversely, the boiler operating cost progressively decreases, from approximately 191 k€/y at the lowest sizing factor to a negligible value at full peak-load coverage, where the boiler is reduced to covering a few residual peak demand events. As a result of these opposing trends, the total annualized cost does not vary monotonically: it first decreases, as the reduction of the boiler contribution outweighs the growth of the heat pump cost, and then rises again at high sizing factors, where the increasing heat pump CAPEX and electricity consumption become dominant.

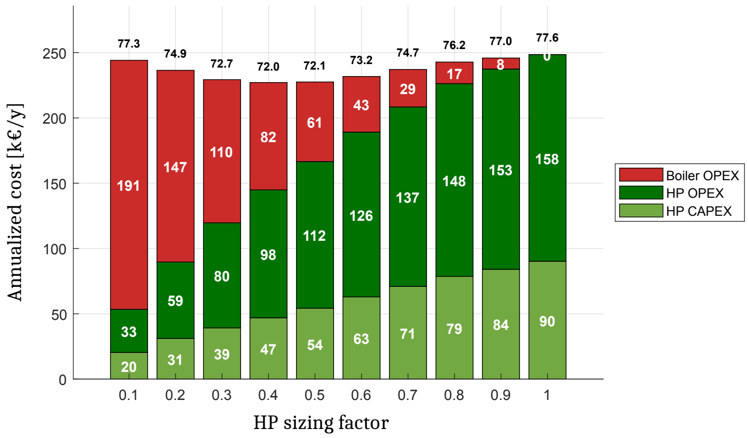


Figure 22: Annual cost of the integrated HP–boiler system as a function of the sizing factor with the LCOH at the top of each bar.

The total levelised cost of heat of the system is also reported above each bar, evaluated for the baseline energy-price scenario (mean gas price of 47.3 €/MWh, without $CO_2$ emission cost). Since the annual heat delivered to the network is essentially independent of the sizing factor, the LCOH mirrors the non-monotonic behaviour of the total annuity: it decreases from 77.3 €/MWh at an HP sizing factor of 0.1 to a minimum of 72.0 €/MWh at a sizing factor of 0.4, and subsequently rises again up to 77.6 €/MWh for complete peak load coverage. This behaviour reflects the competition between two opposing effects: on one hand, increasing the heat pump size displaces an increasing share of expensive boiler gas with cheaper electricity, reducing the specific cost of the heat delivered; on the other hand, beyond a certain size the additional investment and the growing electricity consumption are no longer offset by the marginal gas savings, and the LCOH rises again. The fact that the total system cost decreases over a substantial portion of the power range, despite the higher electricity consumption, indicates that under the present price assumptions the cost of natural gas exerts a stronger influence on the system economics than the cost of electricity. This observation motivates the sensitivity analysis on the energy price scenarios presented in Section 4.2.1.
It is important to distinguish the LCOH trend from that of the absolute system annuity. While the LCOH normalizes the cost with respect to the heat delivered, the absolute annuity reflects the total magnitude of expenditure. A further point of interest emerges from the distribution of individual cost contributions: at high sizing factors, the heat pump OPEX constitutes the dominant share of the total annualized cost, accounting for approximately 64 % of the overall cost under full electrification, while the CAPEX contribution remains comparatively limited. Moreover, the last increments in HP sizing factor mainly serve to eliminate an already marginal boiler contribution, at the expense of a higher initial investment and increased electricity consumption. This behaviour, together with the LCOH minimum observed at intermediate sizing, suggests the existence of an economically optimal size that does not coincide with full peak-load coverage; this aspect is examined in detail

in Section 4.2.1.

Figures 23 and 24 provides a more detailed breakdown of the heat pump investment cost, showing both the percentage share of each component and their absolute contributions as a function of the HP sizing factor. In absolute terms, all components increase consistently with the installed power, as expected from the larger sizing required to process higher thermal and mechanical duties. The compressor is systematically the most economically relevant component, accounting for approximately 45 % to 49 % of the total cost across the entire power range considered. In absolute terms, its cost increases from approximately 63.7 k€ at a sizing factor of 0.1 to over 310 k€ for complete peak load coverage, reflecting the strong dependence of compressor cost on the installed mechanical power.
The evaporator represents the second most significant contribution in absolute terms; however, its relative share progressively decreases from approximately 31 % to 21 % as the installed power increases. This behaviour suggests that downsizing the system penalizes the compressor less than the heat exchangers in relative terms, the latter benefiting from more favourable economies of scale at large sizes. The condenser, by contrast, shows an opposite trend, with its percentage share growing from approximately 5 % to over 12 % of the total cost. This trend can be attributed to the increasing heat transfer area required to comply with the pinch-point constraints imposed in the model at higher thermal duties.
The contribution of the internal heat exchanger is particularly noteworthy. Although the IHX represents the distinctive element of the selected configuration, its economic impact remains relatively limited, staying below 7 % of the total cost across all sizing factors analyzed, and increasing in absolute terms up to 40.6 k€, consistent with the larger refrigerant flow rate to be processed at full power. This result indicates that the increase in plant complexity associated with the introduction of the recuperator is modest relative to the thermodynamic benefits discussed in Section 4.1.2, confirming the overall cost-effectiveness of the SS+IHX solution.
Finally, the costs associated with the balance of plant (BOP), which in this model include maintenance costs, the working fluid receiver located at the condenser outlet, and the cost of the working fluid itself, show relative stability, contributing approximately 11 % of the total cost across the entire HP sizing factor range analyzed and decreasing only marginally. This behaviour suggests good scalability of the auxiliary equipment and confirms that the evolution of the cost structure with increasing power installed is primarily governed by the sizing of the main components of the vapor-compression cycle.

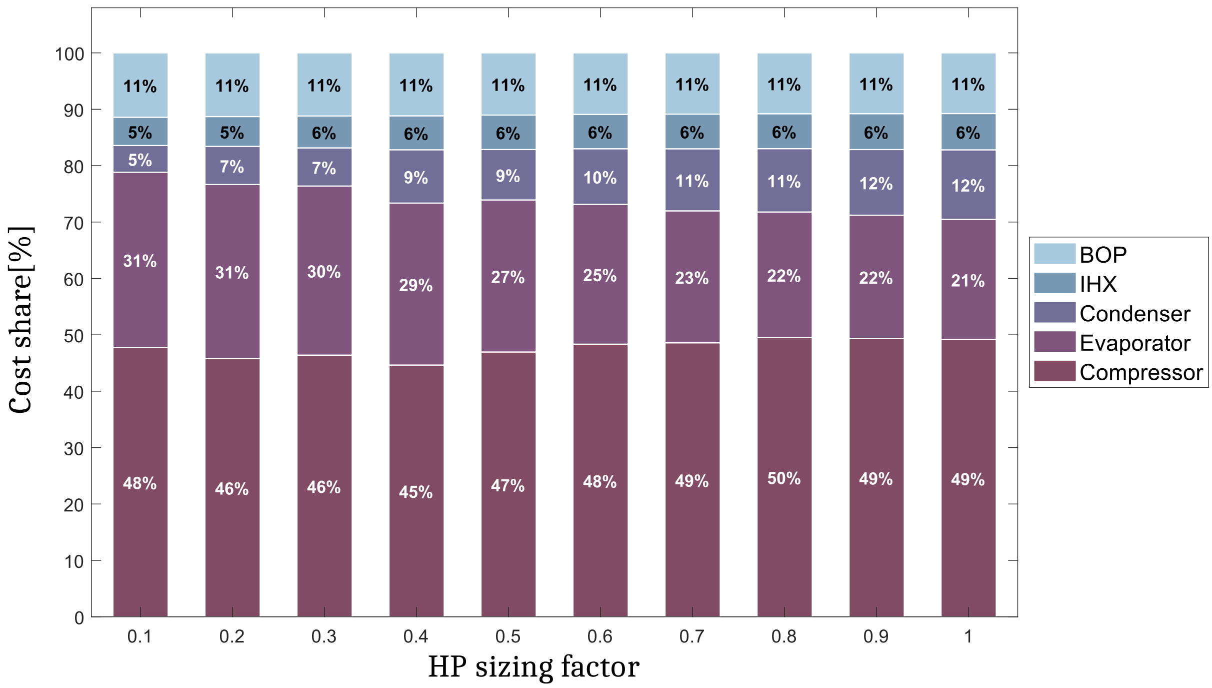


Figure 23: Relative contributions of the main heat pump components to the total investment cost.

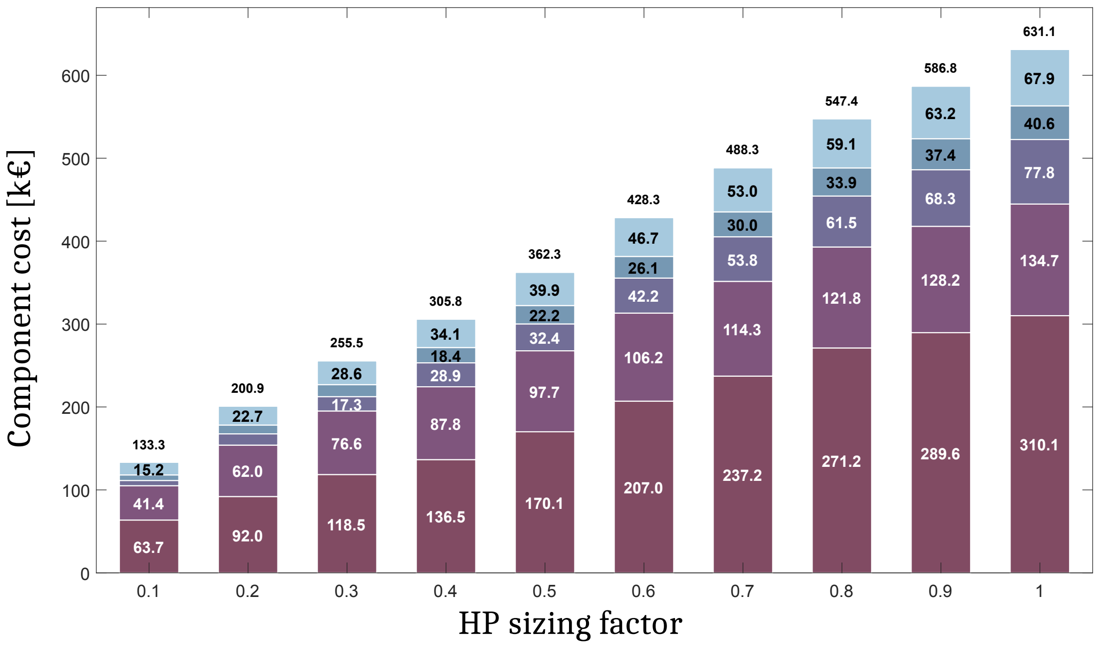


Figure 24: Absolute contributions of the main heat pump components to the total investment cost.

### 4.2.1 Optimal HP sizing factor selection

The selection of the installed heat pump sizing factor was carried out by jointly considering the levelised cost of heat, the annual energy contribution of the heat pump and the auxiliary boiler, and the equivalent operating hours of the machine.

Figure 25 shows the levelised cost of heat of the system as a function of the installed heat pump size, considering different scenarios of natural gas price and $CO_2$ emission cost. The trend of the curves depends considerably on the price scenario considered: for scenarios characterized by higher gas prices (2023, ETS heavy and light), a well-defined economic minimum is observed at low-to-medium installed sizes, whereas for the scenario with the most favourable gas price (2019) the economic advantage of the heat pump over the boiler is less pronounced, and the LCOH remains relatively flat over a wider range of sizes. In all cases, for low values of installed power the system relies heavily on the auxiliary boiler contribution, resulting in an increased specific cost of the heat produced; as the heat pump size increases, reliance on the boiler progressively decreases and the levelised cost decreases accordingly, before rising again once the higher investment costs and increased electricity consumption outweigh the economic benefit of displacing natural gas.

Since the location of the minimum depends on the assumed energy prices, the optimal sizing is defined with reference to the baseline scenario (mean gas price of 47.3 €/MWh, without $CO_2$ emission cost, and mean electricity price of 133.6 €/MWh), corresponding to the grey curve. Under this scenario, the system LCOH reaches its minimum at an HP sizing factor of approximately 0.4. For completeness, the green curve reports the levelised cost of the heat pump alone, excluding the auxiliary boiler: its minimum lies at a slightly lower size, around 2.1 MW (a sizing factor of approximately 0.3), since the heat-pump-only cost favours a smaller, highly utilized machine and is not affected by the boiler gas expenditure. The system optimum is shifted towards a slightly larger size because, accounting also for the boiler operating cost, a larger heat pump displaces a greater share of expensive natural gas. The optimal sizing is therefore established on the basis of the whole-system curve, the heat-pump-only minimum being reported only as an indication; the robustness of this choice with respect to the energy-price assumptions is subsequently assessed in the sensitivity analysis (Figure 30).

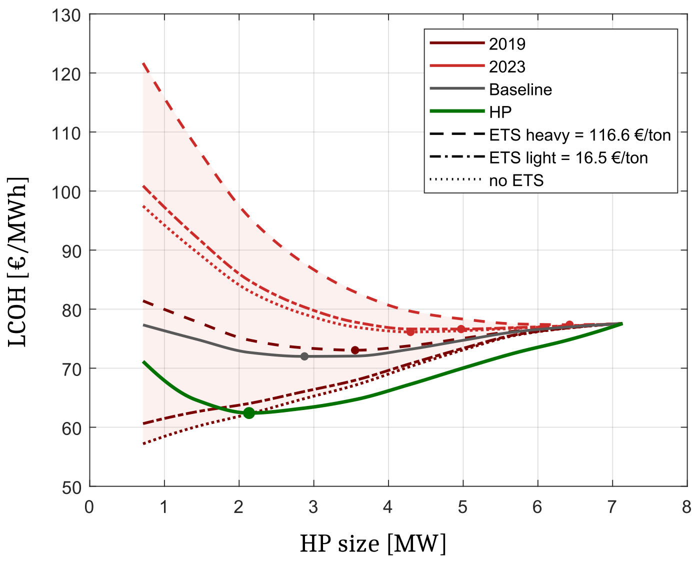


Figure 25: System LCOH as a function of the heat pump size for different natural gas price and $CO_2$ emission cost scenarios; the green curve reports the levelised cost of the heat pump alone.

Figure 26 reports the annual energy contribution provided by the heat pump and the boiler as a function of the HP sizing factor. A heat pump sized to cover 40 % of the peak thermal load is already able to meet approximately 73 % of the annual thermal demand of the district heating network, while a sizing factor of 0.6 allows approximately 89 % of the overall demand to be covered. Further increases in installed power therefore displace progressively smaller shares of the auxiliary boiler contribution, consistently with what is observed in Figure 22, where the boiler contribution becomes negligible for high sizing factors, highlighting a diminishing-returns effect in terms of additional renewable heat supplied.

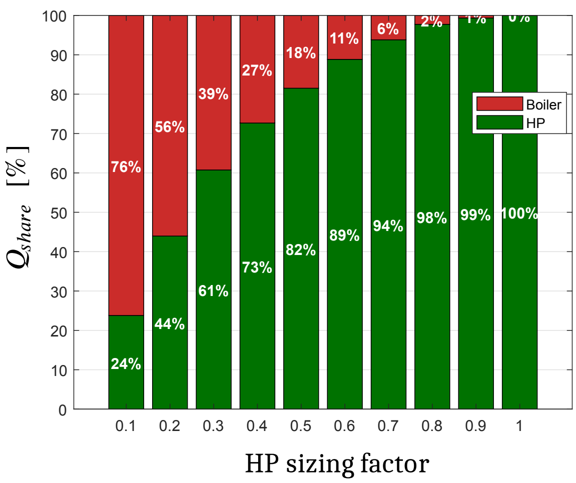


Figure 26: Distribution of annual heat production between the heat pump and the boiler for different sizing factors.

The monthly resolution of the heat pump and boiler contributions at the selected sizing factor ($f_{HP} = 0.6$) is shown in Figure 27, which reports the monthly heat delivered by the heat pump and by the auxiliary boiler over the heating season. The profile spans the period from April 2022 to March 2023, consistently with the annual load data described in Section 2.1; the summer months (May to October), characterized by a negligible thermal demand, are omitted, and the dashed vertical line marks the transition between the two calendar years. The district heating demand follows the expected seasonal profile, rising from approximately 340 MWh at the beginning and end of the season to a maximum of about 770 MWh in the coldest month. Throughout the entire season, the heat pump carries the dominant share of the load, closely tracking the demand profile, while the auxiliary boiler provides only a limited contribution, ranging from approximately 40 MWh to 95 MWh per month and reaching its maximum during the central winter months, when the demand exceeds the installed heat pump power. This monthly breakdown confirms, at finer temporal resolution, the annual coverage discussed above: the heat pump sized at $f_{HP} = 0.6$ is able to meet the largest part of the demand in every month, with the boiler intervening only to cover the peak thermal loads occurring in the coldest period of the year.

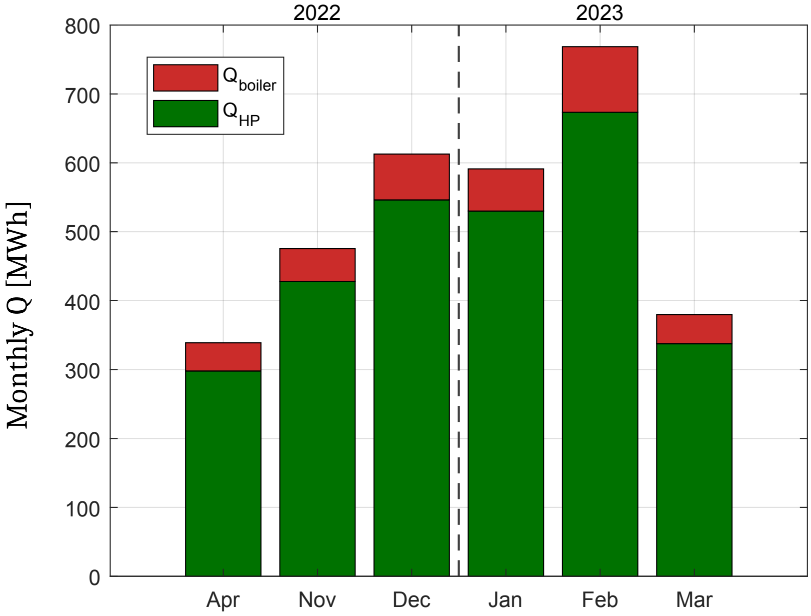


Figure 27: Monthly heat delivered by the heat pump and by the auxiliary boiler over the heating season (April 2022 – March 2023) for the selected sizing factor.

This behaviour is confirmed by the analysis of the equivalent operating hours, reported in Figure 28. As the installed power increases, the equivalent operating hours of the heat pump decrease considerably, ranging from values above 1000 h for low sizing factors to below 500 h for complete peak load coverage. This trend is consistent with the distribution of the annual thermal demand, characterized by high thermal loads occurring for a limited number of hours per year. The load-duration curve indeed shows that a large heat pump would operate at partial load, or even remain idle, for a significant portion of the year, resulting in a reduced utilization factor of the investment.

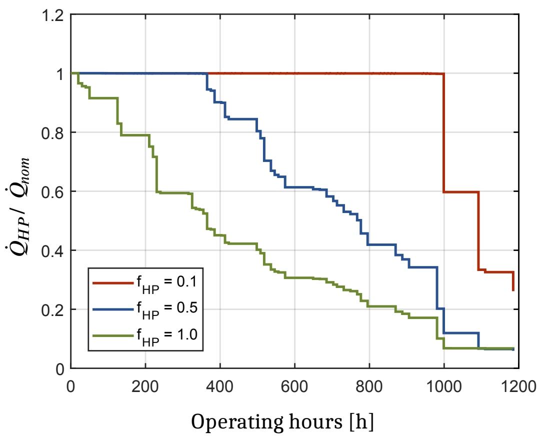


(a) Load-duration curves of the normalized heat pump output for three representative sizing factors.

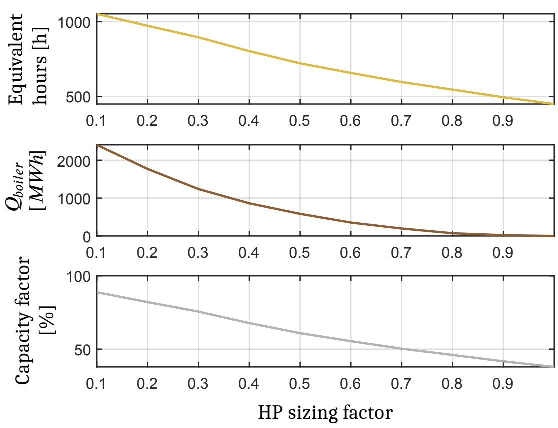


(b) equivalent full-load operating hours (top) and annual auxiliary boiler energy (bottom) as a function of the HP sizing factor.

Figure 28: Equivalent full-load operating hours and auxiliary boiler requirements as a function of the heat pump sizing factor.

The joint analysis of the preceding indicators reveals the existence of an intermediate optimal heat pump size. From a purely economic standpoint, the system LCOH minimum occurs at a sizing factor of approximately 0.4;

this configuration, however, results in a modest renewable coverage, equal to approximately 73 % of the annual demand. Owing to the flat-bottomed shape of the LCOH curve, increasing the sizing factor to approximately 0.6 entails only a marginal rise in the levelised cost of heat, from approximately 72.0 €/MWh to 73.2 €/MWh, corresponding to less than 2 %, while increasing the share of renewable energy delivered to the network from 73 % to 89 % and maintaining an acceptable number of equivalent operating hours. The modest economic penalty associated with this larger size is therefore largely outweighed by the substantial gain in natural gas displacement and decarbonisation potential. A sizing factor of approximately 0.6 is consequently identified as the most advantageous compromise between economic competitiveness, high renewable coverage, and adequate machine utilization.

To complement the economic and energetic criteria discussed above, the environmental benefit associated with the heat pump sizing is examined in Figure 29, which compares three representative sizing factors,a strongly boiler-dominated case ($f_{HP} = 0.1$), the selected optimal case ($f_{HP} = 0.6$), and full peak-load coverage ($f_{HP} = 1.0$), in terms of direct $CO_2$ emissions, annual electricity consumption, and the corresponding electricity cost.
The direct $CO_2$ emissions, originating from the natural gas combustion in the auxiliary boiler, decrease sharply with increasing heat pump sizing factor, falling from approximately 540 t/y at $f_{HP} = 0.1$ to 79 t/y at $f_{HP} = 0.6$, and to zero at full electrification, where the boiler is entirely displaced. The increase in sizing factor from 0.1 to 0.6 therefore already achieves approximately 85 % of the maximum attainable reduction in direct emissions. The residual emissions eliminated by moving from $f_{HP} = 0.6$ to $f_{HP} = 1.0$ are comparatively marginal, and are obtained at the expense of a disproportionate increase in electricity consumption, which rises from approximately 569 MWh/y at the optimal sizing to 676 MWh/y at full coverage, with the annual electricity cost increasing correspondingly from approximately 76 k€/y to 90.3 k€/y.
This behaviour confirms, from an environmental standpoint, the diminishing-returns effect already observed for the economic and energetic indicators: the selected sizing factor of approximately 0.6 captures the large majority of the achievable decarbonisation benefit while avoiding the disproportionate electricity consumption and investment associated with full peak-load coverage.

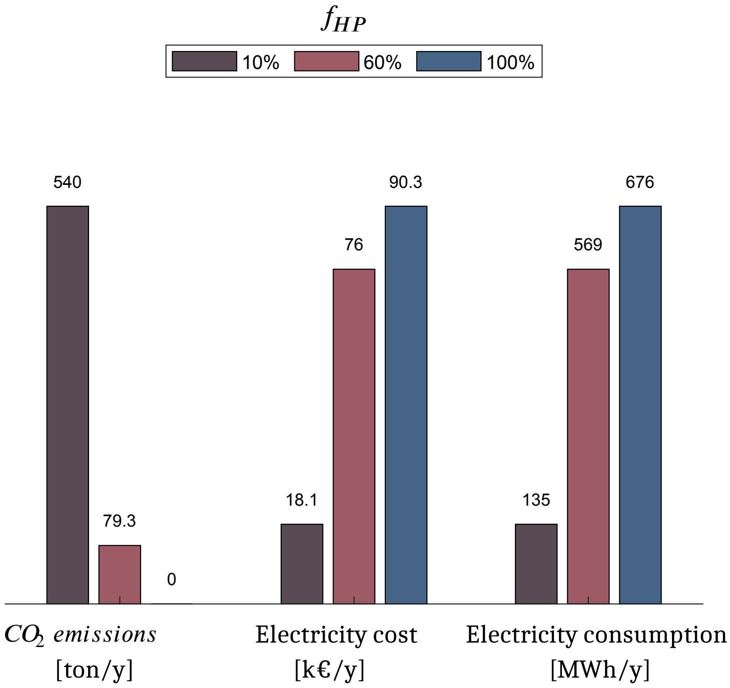


Figure 29: Direct $CO_2$ emissions, annual electricity consumption, and annual electricity cost for three representative sizing factors.

Finally, a sensitivity analysis was carried out to assess the robustness of the optimal sizing with respect to energy market conditions, by varying both the natural gas price and the electricity price across representative scenarios. The results are reported in Figure 30, organised into three panels, each corresponding to a different electricity price scenario.
The analysis shows that the electricity price scenario affects not only the absolute level of the system LCOH, with lower electricity prices yielding proportionally lower curves, but also the location of the economic optimum. The optimal heat pump size is governed not by either energy price in isolation, but by their ratio: the heat pump

is favoured in size to the extent that the electricity it consumes is cheap relative to the gas it displaces. More precisely, the relevant quantity is the ratio between the specific cost of the displaced boiler heat ($c_{\mathrm{fuel}}/\eta_{\mathrm{boiler}}$) and the specific cost of the heat delivered by the heat pump ($c_{\mathrm{el}}/\mathrm{COP}$); since the boiler efficiency and the COP vary only marginally across the sweep, this is well approximated by the gas-to-electricity price ratio.
Consequently, the optimal size increases monotonically with the gas-to-electricity price ratio. Within a fixed gas scenario, lowering the electricity price raises the ratio and shifts the optimum towards larger sizes (e.g. for the 2019 gas price, the system minimum moves from approximately 2.9 MW at the highest electricity price to about 6.4 MW at the lowest); conversely, within a fixed electricity scenario, lowering the gas price reduces the ratio and shifts the optimum towards smaller sizes. Scenarios in which gas and electricity prices lie at matching tiers (both at their 2019, mean, or high levels) leave the ratio approximately unchanged and therefore share a common optimum near 2.9 MW, whereas a one-tier mismatch in favour of gas shifts it to approximately 4.3 MW. At the opposite extreme, when gas is cheap and electricity expensive the unconstrained optimum falls below the smallest simulated size, so that several price pairs (e.g. 2019 gas combined with the mean or 2022 electricity prices) all collapse onto the lower bound of approximately 0.7 MW. The heat-pump-only curve, by contrast, retains its minimum at approximately 2.1 MW regardless of scenario, since by excluding the boiler gas expenditure it is insensitive to the price ratio.
Although the absolute levelised cost and the precise location of the optimum therefore depend appreciably on the energy-price scenario, the flat-bottomed shape of the LCOH curves implies that a sizing factor of approximately 0.6 entails only a marginal economic penalty across the range of plausible market conditions, while securing a substantially higher renewable coverage. The selected sizing factor is thus retained as a robust compromise, not because the economic optimum is stationary, but because the cost surface is shallow around it.

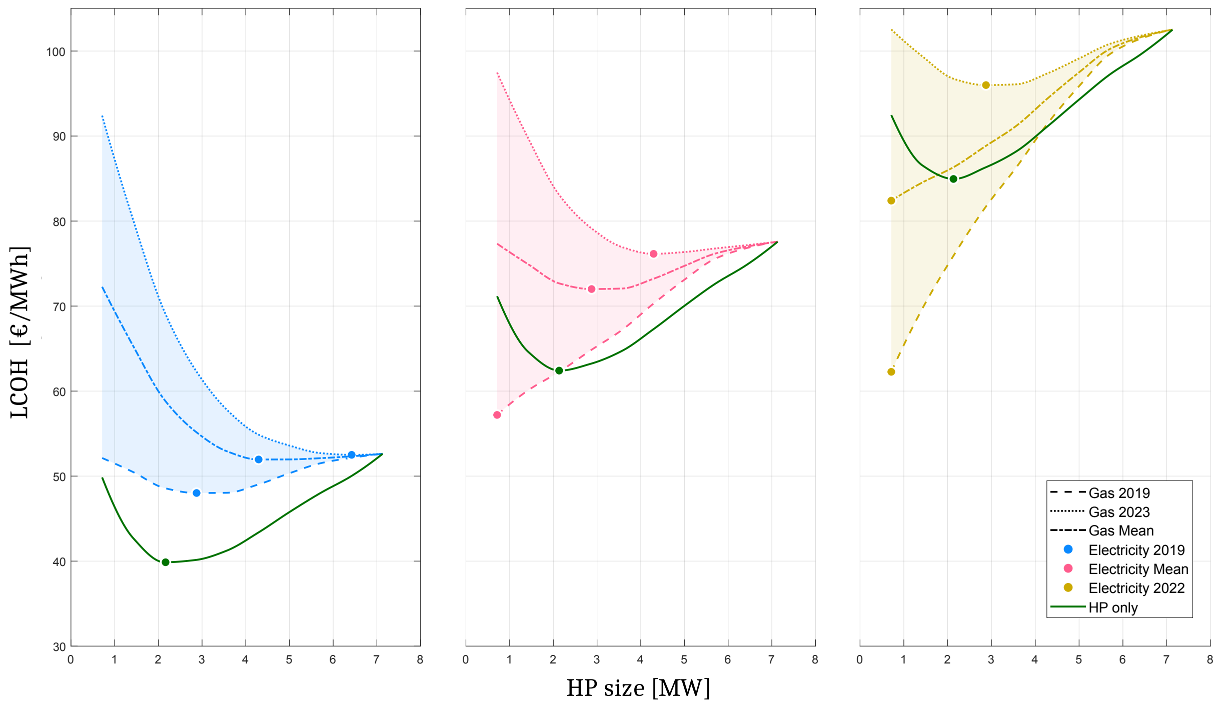


Figure 30: Influence of the natural gas and electricity price scenarios on the system LCOH as a function of the heat pump size. Each panel corresponds to a different electricity price scenario (left: 2019; centre: 2022; right: mean), with the natural gas price varied across its representative range within each panel. The solid green curve reports the levelised cost of the heat pump alone, excluding the auxiliary boiler.

Figure 31 reports the discounted payback time of the SS+IHX configuration with isobutane as a function of the heat pump size, for the different natural gas price and $CO_2$ emission cost scenarios. As for the LCOH, the payback time exhibits a flat-bottomed, non-monotonic dependence on the heat pump size: it decreases at small sizes, where each increment of installed capacity displaces a large share of expensive boiler gas, reaches a minimum at intermediate sizing, and rises again at large sizes, where the additional investment is no longer offset by the marginal gas savings. The absolute level of the payback depends strongly on the price scenario: higher gas prices and higher $CO_2$ costs (2023, ETS heavy) shorten the payback markedly by increasing the value of the displaced natural gas, whereas the most favourable gas price (2019, no ETS) yields the longest payback. Across all scenarios, the minimum-payback size coincides with the size that minimizes the heat-pump-only LCOH (green curve in Figure 30), rather than with the system-LCOH minimum. This is consistent with the fact that the payback is governed by the savings generated by the heat pump investment relative to the all-boiler reference case. This minimum lies at approximately 2.1 MW (a sizing factor of about 0.3), slightly below the size selected on the basis of the joint analysis of system LCOH, renewable coverage, and equivalent operating hours. In the least favourable price scenarios the payback approaches the 20-year evaluation horizon (horizontal line), whereas under carbon-priced conditions it falls to roughly 5 years, well within the plant lifetime.

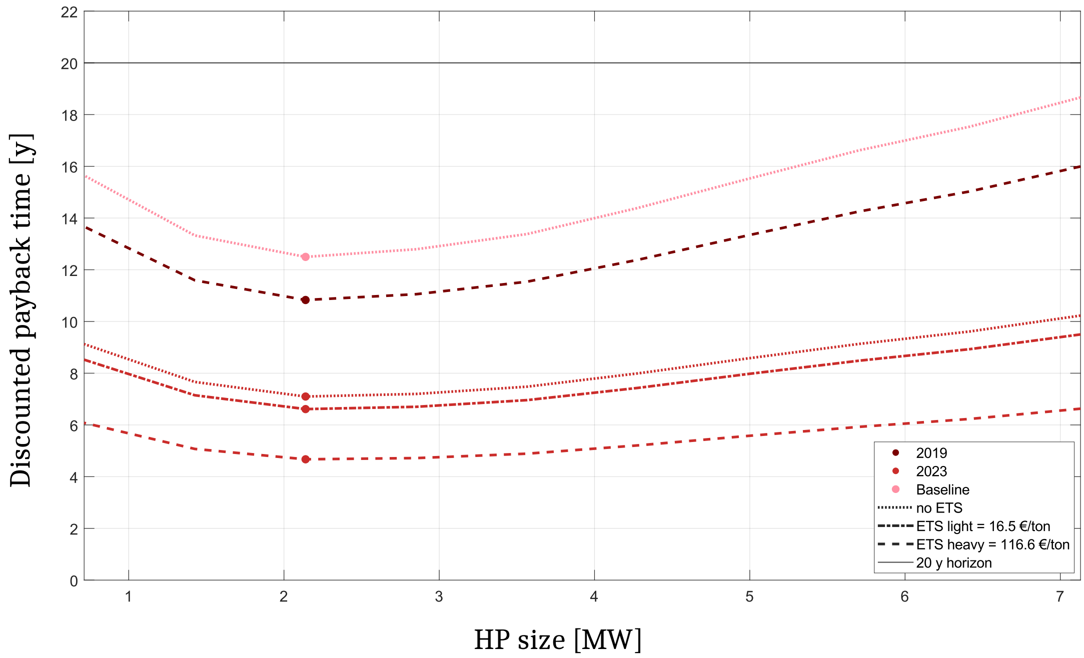


Figure 31: Discounted payback time of the SS+IHX configuration with isobutane as a function of the heat pump size, for the different natural gas price and $CO_2$ emission cost scenarios. The payback is computed against the all-boiler reference case; the horizontal line marks the 20-year evaluation horizon.

## 5. Conclusion

This work presented a techno-economic assessment and optimal sizing study of a large-scale high-temperature heat pump integrated into the geothermal district heating system of the Isar Valley. Three cycle architectures: a single-stage cycle (SS), a single-stage cycle with internal heat exchanger (SS+IHX), and a two-stage cascade cycle, were compared under identical boundary conditions, each coupled with a screening of low-GWP working fluids and an annual thermodynamic simulation over the full 8760-hour load profile, followed by a unified LCOH-based economic evaluation including an auxiliary natural gas boiler covering the residual load.

**Comparison of the configurations.** The three configurations were found to deliver comparable thermodynamic performance at the design point, but to differ appreciably on the economic side. The introduction of the internal heat exchanger improved the coefficient of performance of every refrigerant with respect to the reference single-stage cycle, while adding only a limited investment, the IHX accounting for less than 7 % of the heat pump capital cost across the whole sizing range. The two-stage cascade configuration, by contrast, did not prove competitive for the present application: at the moderate temperature lift characterizing this geothermal source, the thermodynamic benefit of two-stage compression, which becomes significant only for large lifts, does not offset the additional cost of the second compressor and the cascade heat exchanger, resulting in a substantially higher levelised cost of heat. The SS+IHX cycle therefore emerged as the most favourable compromise between cycle efficiency and capital expenditure. The same ranking held for the discounted payback time: the SS+IHX cycle amortised the heat pump investment in approximately 18 years under baseline prices, the shortest of the three configurations, against 22 years for the single-stage and 33 years for the cascade, decreasing to roughly 5 years once $CO_2$ pricing is accounted for.

**Role of the working fluid.** Across all configurations, hydrocarbons consistently provided the best economic performance, combining a competitive COP with a low capital cost. In the single-stage cycle butane

(R600) yielded the lowest LCOH (85.9 €/MWh), while in the SS+IHX configuration isobutane (R600a) became the most cost-effective fluid, with a preliminary LCOH of 77.5 €/MWh, a design-point COP of 4.45, and an optimal recuperator temperature difference of 11 K resulting from the trade-off between efficiency gain and additional investment. Butane remained essentially equivalent to isobutane, the difference between the two being below 2 %. The higher-critical-temperature fluids, despite occasionally competitive COP values, were systematically penalized by higher capital costs. For the cascade configuration, the propane/butane pairing achieved the lowest LCOH among the combinations investigated.

**Heat pump sizing.** On the basis of these results, the SS+IHX cycle with isobutane was selected for a detailed sizing study, in which the installed heat pump power was progressively reduced and the residual load assigned to the auxiliary boiler. With reference to the baseline energy-price scenario, the system levelised cost of heat exhibited a flat-bottomed, non-monotonic dependence on the heat pump size, reaching its minimum of approximately 72.0 €/MWh at a sizing factor of about 0.4. However, when the levelised cost of heat is considered jointly with the share of renewable energy delivered to the network and the equivalent operating hours of the heat pump, a sizing factor of approximately 0.6 was identified as the most advantageous compromise: it raises the LCOH by less than 2 % with respect to its minimum, while increasing the annual renewable coverage from approximately 73 % to 89 % and almost eliminating the direct $CO_2$ emissions of the auxiliary boiler. Beyond this size, further sizing factors increments yield rapidly diminishing returns, displacing only a marginal residual boiler contribution at the expense of a disproportionate rise in investment and electricity consumption. A sensitivity analysis on the natural gas and electricity prices confirmed that the absolute levelised cost depends markedly on the energy-price scenario, and showed that the location of the economic optimum is governed by the ratio between the specific cost of the displaced boiler heat and that of the heat delivered by the heat pump: the optimal size increases monotonically with the gas-to-electricity price ratio, ranging from the smallest simulated size when gas is cheap and electricity expensive, up to roughly 6.4 MW in the opposite case. Nevertheless, owing to the flat-bottomed shape of the LCOH curves, the selected sizing factor of approximately 0.6 entails only a marginal economic penalty across the full range of scenarios considered, and therefore remains a robust compromise between cost, renewable coverage, and heat pump utilization.

**Limitations and future developments.** The present analysis is subject to a number of limitations that also indicate directions for further work. The economic boundary was restricted to the heat pump and the operating cost of the auxiliary boiler, excluding the capital cost of the boiler and the costs associated with well drilling, the brine extraction pump, and the primary heat exchanger; a more complete techno-economic boundary would allow an absolute, rather than comparative, assessment of the plant, which is necessary for completely new installations. The thermodynamic model is steady-state and based on representative typedays, so that transient effects, start-up and shut-down dynamics, and part-load control strategies are not captured. The refrigerant screening, although covering the most promising low-GWP candidates, could be extended to additional fluids and to further cascade pairings. Finally, the integration of thermal energy storage, the inclusion of a reversible operating mode, and the assessment of the system under future scenarios of electricity and carbon prices represent promising extensions, potentially shifting the balance between heat pump and boiler and further improving the decarbonisation potential of the integrated system.

## 6. Bibliography and citations

## References


[1] Unfccc. ADOPTION OF THE PARIS AGREEMENT - Paris Agreement text English. Technical report.

[2] Energy Statistics Data Browser – Data Tools - IEA.

[3] IPCC. Global Warming of 1.5°C.An IPCC Special Report on the impacts of global warming of 1.5°C above pre-industrial levels and related global greenhouse gas emission pathways, in the context of strengthening the global response to the threat of climate change, 2018.

[4] Cordin Arpagaus, Frédéric Bless, Michael Uhlmann, Jürg Schiffmann, and Stefan S. Bertsch. High temperature heat pumps: Market overview, state of the art, research status, refrigerants, and application potentials, 6 2018.

[5] F. Schlosser, M. Jesper, J. Vogelsang, T. G. Walmsley, C. Arpagaus, and J. Hesselbach. Large-scale heat pumps: Applications, performance, economic feasibility and industrial integration. *Renewable and Sustainable Energy Reviews*, 133, 11 2020.

[6] Sven Werner. District heating and cooling in Sweden. *Energy*, 126:419–429, 5 2017.

[7] Simone Buffa, Marco Cozzini, Matteo D'Antoni, Marco Baratieri, and Roberto Fedrizzi. 5th generation district heating and cooling systems: A review of existing cases in Europe. *Renewable and Sustainable Energy Reviews*, 104:504–522, 4 2019.

[8] Bayerische Staatskanzlei. Bayerisches Gesetz- und Verordnungsblatt Nr. 24-2024. Technical report.

[9] Jaromir Jeßberger, Florian Heberle, and Dieter Brüggemann. Maximising the potential of deep geothermal energy: Thermal output increase by large-scale heat pumps. *Applied Thermal Engineering*, 257, 12 2024.

[10] Florian Kaufmann, Hartmut Spliethoff, and Christopher Schifflechner. Reversible high-temperature heat pumps for peak load coverage in geothermal heating plants: A techno-economic analysis. *Energy Conversion and Management*, 347, 1 2026.

[11] Oguz Arslan, Asli Ergenekon Arslan, and Irfan Kurtbas. Exergoeconomic and exergoenvironmental based multi-criteria optimization of a new geothermal district heating system integrated with thermal energy storage driven heat pump. *Journal of Building Engineering*, 73, 8 2023.

[12] Jiewen Deng, Yangyang Su, Chenwei Peng, Wenbo Qiang, Wanlong Cai, Qingpeng Wei, and Hui Zhang. How to improve the energy performance of mid-deep geothermal heat pump systems: Optimization of heat pump, system configuration and control strategy. *Energy*, 285, 12 2023.

[13] Carlos Mateu-Royo, Cordin Arpagaus, Adrián Mota-Babiloni, Joaquín Navarro-Esbrí, and Stefan S. Bertsch. Advanced high temperature heat pump configurations using low GWP refrigerants for industrial waste heat recovery: A comprehensive study. *Energy Conversion and Management*, 229, 2 2021.

[14] Adrián Mota-Babiloni, Carlos Mateu-Royo, Joaquín Navarro-Esbrí, Francisco Molés, Marta Amat-Albuixech, and Ángel Barragán-Cervera. Optimisation of high-temperature heat pump cascades with internal heat exchangers using refrigerants with low global warming potential. *Energy*, 165:1248–1258, 12 2018.

[15] George Kosmadakis, Cordin Arpagaus, Panagiotis Neofytou, and Stefan Bertsch. Techno-economic analysis of high-temperature heat pumps with low-global warming potential refrigerants for upgrading waste heat up to 150 °C. *Energy Conversion and Management*, 226, 12 2020.

[16] Pullach | Informationsportal Tiefe Geothermie.

[17] Jaromir Jeßberger, Hannah Uhrmann, Felix Schölderle, Daniela Pfrang, Florian Heberle, Kai Zosseder, and Dieter Brüggemann. Medium-deep geothermal resources in the Molasse Basin: A geological, techno-economic, and ecological study of large-scale heat pump integration. *Renewable Energy*, 248, 8 2025.

[18] Tiefe Geothermie - Ausbau & Entwicklung.

[19] Geothermal heat production, deep (>1500<4000 meter) - Energy.nl.

[20] J. Barco-Burgos, J. C. Bruno, U. Eicker, A. L. Saldaña-Robles, and V. Alcántar-Camarena. Review on the integration of high-temperature heat pumps in district heating and cooling networks. *Energy*, 239, 1 2022.

[21] Wetter und Klima - Deutscher Wetterdienst - CDC (Climate Data Center).

[22] Guido Francesco Frate, Lorenzo Ferrari, and Umberto Desideri. Analysis of suitability ranges of high temperature heat pump working fluids. *Applied Thermal Engineering*, 150:628–640, 3 2019.

[23] Mattias Nilsson, Harald Nes Rislå, and Konstantinos Kontomaris. Measured performance of a novel high temperature heat pump with HFO-1336mzz(Z) as the working fluid. Technical report.

[24] Jason R Juhasz. Novel Working Fluid, HFO-1336mzz(E), for Use in Waste Heat Recovery Application. Technical report.

[25] A NON-FLAMMABLE, ZERO-ODP, LOW GWP WORKING FLUID FOR HIGH TEMPERATURE HEAT PUMPS: DR-148. Technical report.

[26] M. P. Bertinat. Fluids for high temperature heat pumps. *International Journal of Refrigeration*, 9(1):43–50, 1 1986.

[27] Selahattin Göktun. Selection of working fluids for high-temperature heat pumps. *Energy*, 20(7):623–625, 7 1995.

[28] O. Kleefkens and S. Spoelstra. R&D on Industrial Heat Pumps. *11th IEA Heat Pump Conference 2014*, pages 1–10, 7 2014.

[29] Regulation (EC) No 1005/2009 of the European Parliament and of the Council of 16 September 2009 on substances that deplete the ozone layer.

[30] The European Parliament and the Council of the European, Union. Regulation (EU).No 517/2014 of the European Parliament and the Council of 16 April 2014 on fluorinatedgreenhousegasesandrepealingRegulation(EC). No842/2006OffJEurUnion 150, 195–230 2014.

[31] K. O. Patten and D. J. Wuebbles. Atmospheric lifetimes and Ozone Depletion Potentials of trans-1-chloro-3,3,3-trifluoropropylene and trans-1,2-dichloroethylene in a three-dimensional model. *Atmospheric Chemistry and Physics*, 10(22):10867–10874, 2010.

[32] Björn Palm. Hydrocarbons as refrigerants in small heat pump and refrigeration systems – A review. *International Journal of Refrigeration*, 31(4):552–563, 6 2008.

[33] Adrián Mota-Babiloni, Joaquín Navarro-Esbrí, Ángel Barragán, Francisco Molés, and Bernardo Peris. Drop-in energy performance evaluation of R1234yf and R1234ze(E) in a vapor compression system as R134a replacements. *Applied Thermal Engineering*, 71(1):259–265, 10 2014.

[34] Eric W. Lemmon, Marcia L. Huber, and Mark O. McLinden. NIST Standard Reference Database 23: Reference Fluid Thermodynamic and Transport Properties-REFPROP, Version 9.1, 2013.

[35] Florian Kaufmann, Ludwig Irrgang, Christopher Schifflechner, and Hartmut Spliethoff. Fast and accurate modelling of twin-screw compressors: A generalised low-order approach. *Applied Thermal Engineering*, 257:124238, 12 2024.

[36] Konstantinos Braimakis and Sotirios Karellas. Integrated thermoeconomic optimization of standard and regenerative ORC for different heat source types and capacities. *Energy*, 121:570–598, 2017.

[37] Vdi. VEREIN DEUTSCHER INGENIEURE Referenzlastprofile von Ein-und Mehrfamilien-häusern für den Einsatz von KWK-Anlagen Reference load profiles of single-family and multi-family houses for the use of CHP systems VDI-RICHTLINIEN. 2008.

[38] Marco Astolfi, Matteo C. Romano, Paola Bombarda, and Ennio Macchi. Binary ORC (Organic Rankine Cycles) power plants for the exploitation of medium-low temperature geothermal sources - Part B: Techno-economic optimization. *Energy*, 66:435–446, 3 2014.

[39] Daniël Walraven, Ben Laenen, and William D'haeseleer. Economic system optimization of air-cooled organic Rankine cycles powered by low-temperature geothermal heat sources. *Energy*, 80:104–113, 2 2015.

[40] Torben Ommen, Jonas Kjær Jensen, Wiebke Brix Markussen, Lars Reinholdt, and Brian Elmegaard. Technical and economic working domains of industrial heat pumps: Part 1 – Single stage vapour compression heat pumps. *International Journal of Refrigeration*, 55:168–182, 7 2015.

[41] Adrian. Bejan, G.. Tsatsaronis, and Michael J.. Moran. *Thermal design and optimization*. Wiley, 1996.

[42] VDI - The Association of German Engineers. Economic efficiency of building installations - Fundamentals and economic calculation. (VDI 2067 Blatt 1). DIN Media GmbH; 2012.

[43] Average Spot Market Prices | Energy-Charts.

[44] Germany - Gas prices: Non-household, medium size consumers - 2026 Data 2027 Forecast 2009-2024 Historical.

[45] Carbon Pricing Dashboard | Up-to-date overview of carbon pricing initiatives.

[46] Market Data Hub | EEX.

[47] Antonio Giuffrida. A semi-empirical method for assessing the performance of an open-drive screw refrigeration compressor. *Applied Thermal Engineering*, 93:813–823, 1 2016.

[48] Holger Martin. N6 Pressure Drop and Heat Transfer in Plate Heat Exchangers. In *VDI Heat Atlas*, pages 1515–1522. Springer Berlin Heidelberg, Berlin, Heidelberg, 2010.

# A. Compressor model

The compressor model adopted in the present work is based on the generalized low-order approach proposed by Kaufmann et al. [35], developed from the semi-empirical formulation originally introduced by Giuffrida [47]. The latter accounts for the main physical phenomena occurring inside a twin-screw compressor, including internal leakage, heat transfer between the working fluid and the compressor, mechanical losses, and the effects associated with the built-in volume ratio (BVR). In order to reduce the computational burden and allow extensive annual simulations with integrated optimization, the generalized polynomial formulation proposed by Kaufmann et al. has been applied in the present work.

## Input normalization

The compressor behaviour is described as a function of the volumetric suction flow rate and the external pressure ratio. To extend the applicability of the model to compressors with different swept volumes and built-in volume ratios, these quantities are normalised as follows.
The normalised suction flow rate is defined as:

$$\dot{V}_{\mathrm{suc},N} = \frac{\dot{V}_{\mathrm{suc}}}{V_s \cdot n_{\mathrm{ref}}} \tag{17}$$

where $\dot{V}_{\mathrm{suc}}$ is the volumetric flow rate at the compressor suction port, $V_s$ is the swept volume per shaft revolution, and $n_{\mathrm{ref}} = 50$ Hz (equivalent to 3000 rpm) is the reference rotational speed adopted.
The normalised external pressure ratio is:

$$r_{p,N} = \frac{r_p}{\mathrm{BVR}} \tag{18}$$

where the external pressure ratio is:

$$r_p = \frac{p_{\mathrm{out}}}{p_{\mathrm{in}}} \tag{19}$$

with $p_{\mathrm{out}}$ and $p_{\mathrm{in}}$ denoting the compressor discharge and suction pressures, respectively. A BVR of 3.1 is adopted in this work for the SS and SS+IHX configurations, corresponding to the value used by Kaufmann et al. in the model development.

## Polynomial regressions

The model employs three distinct polynomial regressions to estimate, respectively, the ratio $r_{v,p}$ between the applied volume ratio and the applied pressure ratio, the volumetric efficiency $\eta_{\mathrm{vol}}$, and the isentropic efficiency $\eta_{\mathrm{is}}$. The three polynomials have different orders, selected to minimize the number of coefficients while ensuring a good fit and physically correct behaviour outside the fitting range.

**Ratio $r_{v,p}$.** A polynomial of order 5 in $\dot{V}_{\mathrm{suc},N}$ and order 3 in $r_{p,N}$ is used to estimate the ratio between the applied volume ratio and the applied pressure ratio:

$$r_{v,p} = f\left(\dot{V}_{\mathrm{suc},N},\ r_{p,N}\right) \tag{20}$$

The applied volume ratio is then obtained as:

$$r_v = r_{v,p} \cdot r_p \tag{21}$$

and subsequently normalized:

$$r_{v,N} = \frac{r_v}{\mathrm{BVR}} \tag{22}$$

**Volumetric efficiency.** A polynomial of order 5 in $\dot{V}_{\mathrm{suc},N}$ and order 4 in $r_p$ yields the volumetric efficiency:

$$\eta_{\mathrm{vol}} = f\left(\dot{V}_{\mathrm{suc},N},\ r_p\right) \tag{23}$$

Note that the pressure ratio is not normalized by the BVR for this polynomial, since the driving force for internal leakage is the external pressure ratio $r_p$ regardless of the BVR.

**Isentropic efficiency.** A polynomial of order 2 in $\dot{V}_{\mathrm{suc},N}$ and order 4 in $r_{v,N}$ estimates the isentropic efficiency:

$$\eta_{\mathrm{is}} = f\left(\dot{V}_{\mathrm{suc},N},\, r_{v,N}\right) \tag{24}$$

The polynomial coefficients were determined by Kaufmann et al. by regression over a large synthetic dataset generated from the semi-empirical reference model and are reported in [35]; they are not reproduced here for brevity.

## Regularisation

In order to ensure physically meaningful predictions over the full operational range, the model implements two distinct regularisation procedures.

**Upper-boundary regularisation on $r_{v,N}$.** For values of $r_{v,N}$ exceeding the threshold $r'_{v,N} = 1.3379$, the polynomial isentropic efficiency is replaced by a linear extrapolation in the $r_{v,N}$ direction:

$$\eta_{\mathrm{is,lin}} = \eta_{\mathrm{is}}\left(\dot{V}_{\mathrm{suc},N},\, r'_{v,N}\right) + \frac{\partial \eta_{\mathrm{is}}}{\partial r_{v,N}}\left(\dot{V}_{\mathrm{suc},N},\, r'_{v,N}\right) \cdot \left(r_{v,N} - r'_{v,N}\right) \tag{25}$$

This linearization prevents the unphysical behaviour that a fourth-order polynomial would produce at high pressure ratios.

**Lower-boundary regularisation on $r_p$.** For values of $r_p$ within the interval $[r_{p,\mathrm{min}},\, r_{p,\mathrm{max}}] = [1.0,\, 1.7]$, the isentropic efficiency is blended with a sigmoidal function towards the minimum value $\eta_{\mathrm{is,min}} = 10\,\%$, ensuring a smooth transition at low pressure ratios:

$$\eta_{\mathrm{is}} = (1-\lambda)\,\eta_{\mathrm{is,min}} + \lambda\,\eta_{\mathrm{is,poly}} \tag{26}$$

where $\lambda = 0.5 + 0.5\sin\!\left(\frac{\pi}{2}\frac{r_p}{\varepsilon}\right)$ and $\varepsilon = \frac{r_{p,\mathrm{max}} - r_{p,\mathrm{min}}}{2}$.

## Performance calculation

Once the volumetric efficiency is known, the compressor rotational speed is determined as:

$$n = \frac{\dot{V}_{\mathrm{suc}}}{V_s\,\eta_{\mathrm{vol}}} \cdot 60 \tag{27}$$

The speed is constrained to the operational range $[n_{\mathrm{min}},\, n_{\mathrm{max}}] = [500,\, 4500]$ rpm, which represents the physical limits of the machine and constitutes an explicit constraint enforced within the optimization routine at each simulation time step.
The specific outlet enthalpy is subsequently calculated from the isentropic efficiency definition:

$$h_{\mathrm{out}} = h_{\mathrm{in}} + \frac{h_{\mathrm{out,is}} - h_{\mathrm{in}}}{\eta_{\mathrm{is}}/100} \tag{28}$$

where $h_{\mathrm{out,is}}$ is the specific enthalpy corresponding to an ideal isentropic compression process, evaluated via REFPROP [34] from the discharge pressure and the suction entropy.
The compressor shaft power is finally obtained as:

$$P_{\mathrm{shaft}} = \dot{m}\left(h_{\mathrm{out}} - h_{\mathrm{in}}\right) \tag{29}$$

where $\dot{m}$ is the refrigerant mass flow rate. The electrical power drawn by the compressor drive is obtained by dividing $P_{\mathrm{shaft}}$ by the electro-mechanical efficiency of the motor, assumed to be $\eta_{\mathrm{el}} = 0.95$.
The proposed methodology provides an accurate representation of twin-screw compressor performance while maintaining a substantially lower computational cost compared to semi-empirical or geometry-based models, making it particularly suitable for annual simulations and thermo-economic optimization studies.

# B. Heat exchanger sizing methodology

This appendix describes the methodology implemented for the sizing of the plate heat exchangers used in the heat pump cycle model. The same general numerical framework is adopted for the evaporator, the condenser, the cascade heat exchanger and the internal heat exchanger (IHX). Component-specific differences are introduced only in the definition of the hot and cold streams and in the correlations used when evaporation or condensation occurs.

The sizing routines are based on a discretized plate heat exchanger model, the general approach follows the method of Braimakis et al. [36], while the single-phase heat transfer and pressure drop calculation uses the formulation explained in the VDI [48].

Four heat exchangers are sized:

- the heat pump evaporator;
- the heat pump condenser;
- the internal heat exchanger (IHX);
- the cascade heat exchanger, which works as condenser for the low-stage cycle and as evaporator for the high-stage cycle.

Each plate heat exchanger is described by the vector

$$\mathbf{x} = \begin{bmatrix} L & W & N_p \end{bmatrix}, \tag{30}$$

where $L$ is the plate length, $W$ is the plate width and $N_p$ is the number of plates. The heat transfer area available in the exchanger is calculated as

$$A_{\mathrm{HXs}} = LW(N_p - 2). \tag{31}$$

The objective function returns the required heat transfer area $A_{\mathrm{req}}$ calculated by the detailed heat exchanger model. The optimization imposes that the installed area and the required area are equal, and that the pressure drop remains below the prescribed limit. The equality constraint is written as

$$c_{\mathrm{eq}} = \frac{A_{\mathrm{HXs}} - A_{\mathrm{req}}}{A_{\mathrm{HXs}}} = 0. \tag{32}$$

For single-sided pressure drop constraints, the inequality is

$$c = (\Delta p - 0.1)\,100 \leq 0, \tag{33}$$

where $\Delta p$ is expressed in bar. For two-sided components, such as the cascade heat exchanger, the same constraint is applied separately to the hot and cold sides.

The geometrical and model parameters used in the code are listed in Table 6 [36, 48].

Table 6: Geometrical and model parameters adopted for the plate heat exchanger sizing.

| Parameter | Symbol | Value | Unit |
|---|---|---|---|
| Chevron angle | $\phi$ | 60 | ° |
| Plate thickness | $s$ | 0.0008 | m |
| Plate spacing | $d_p$ | 0.0022 | m |
| Corrugation wavelength | $\Lambda$ | 0.013 | m |
| Corrugation amplitude | $a_m$ | 0.0025 | m |
| Wall thermal conductivity | $k_{\mathrm{wall}}$ | 0.0165 | kW/(m K) |
| Fouling resistance | $R_f$ | 0.000025 | $\mathrm{m^2\,K/kW}$ |
| Number of discretization slices | $N_{\mathrm{slices}}$ | 100 | – |

The heat transfer area of one plate is

$$A_p = LW, \tag{34}$$

and the flow area is

$$A_{\mathrm{flow}} = d_p W. \tag{35}$$

The heat exchanger is discretized into 100 slices. In each slice, local thermodynamic properties, temperature differences, heat transfer coefficients and pressure losses are evaluated. For refrigerant streams, the enthalpy is linearly discretized between inlet and outlet:

$$h_i = h_{\mathrm{in}} + \frac{i}{N_{\mathrm{slices}}}\left(h_{\mathrm{out}} - h_{\mathrm{in}}\right), \qquad i = 0, \ldots, N_{\mathrm{slices}}. \tag{36}$$

The number of channels assigned to each side is approximated as

$$N_{\text{ch,side}} = \frac{N_p}{2}. \tag{37}$$

The volumetric flow rate in one channel is

$$\dot{V}_{\text{ch}} = \frac{\dot{m}/\rho}{N_p/2}, \tag{38}$$

and the mean velocity between two plates is

$$w = \frac{\dot{V}_{\text{ch}}}{2a_m W}. \tag{39}$$

The Reynolds number is

$$Re = \frac{\rho w d_h}{\eta}, \tag{40}$$

where $\rho$ is density, $\eta$ is dynamic viscosity and $d_h$ is the hydraulic diameter.
The Nusselt number is calculated with the modified Leveque-type equation, so that the local convective heat transfer coefficient is

$$\alpha = \frac{Nu\lambda}{d_h}, \tag{41}$$

where $\lambda$ is the thermal conductivity.
The length-specific pressure loss is

$$\frac{\Delta p}{L} = \frac{\xi \rho w^2}{2d_h}. \tag{42}$$

where $\xi$ is the friciton factor. The total pressure drop is obtained by multiplying the mean length-specific pressure loss by the plate length.

When the refrigerant is in the two-phase evaporation region, the heat transfer coefficient is calculated from a single-phase liquid reference coefficient corrected by a boiling number. The latent heat is

$$h_{\text{evap}} = h_{\text{sat,v}} - h_{\text{sat,l}}. \tag{43}$$

The heat flux density used in the code is

$$\dot{q} = \frac{\sum_i \dot{Q}_i / N_p}{A_p}, \tag{44}$$

and the boiling number is

$$Bo_{\text{ev}} = \frac{\dot{q}}{\left[\left(\dot{m}/N_p\right)/A_{\text{flow}}\right] h_{\text{evap}}}. \tag{45}$$

For each slice, the overall heat transfer coefficient is computed by adding the thermal resistances of the two convective sides, the wall and the fouling layer:

$$U_i = \left( \frac{1}{\alpha_{\text{hot},i}} + \frac{s}{k_{\text{wall}}} + \frac{1}{\alpha_{\text{cold},i}} + R_f \right)^{-1}. \tag{46}$$

The required area of each slice is

$$A_i = \frac{\dot{Q}_i}{U_i \Delta T_{\text{lm},i}}, \tag{47}$$

The total required area is

$$A_{\text{req}} = \sum_{i=1}^{N_{\text{slices}}} A_i. \tag{48}$$

The mean logarithmic temperature difference is the arithmetic mean of the slice values:

$$\Delta T_{\text{lm,mean}} = \frac{1}{N_{\text{slices}}} \sum_{i=1}^{N_{\text{slices}}} \Delta T_{\text{lm},i}. \tag{49}$$

The mean overall heat transfer coefficient is reconstructed from the total heat duty:

$$U_{\text{mean}} = \frac{\dot{Q}_{\text{tot}}}{A_{\text{req}} \Delta T_{\text{lm,mean}}}. \tag{50}$$

### Internal volume and refrigerant inventory

The volume of one channel is

$$V_{\text{ch}} = L W d_p. \tag{51}$$

For one side of the heat exchanger, the total internal volume is

$$V_{\text{side}} = \frac{N_p}{2} V_{\text{ch}}. \tag{52}$$

The refrigerant mass contained in the heat exchanger is evaluated slice by slice:

$$m_{\text{HX}} = \sum_{i=1}^{N_{\text{slices}}} \rho_i \frac{V_{\text{side}}}{N_{\text{slices}}}. \tag{53}$$

For two-sided refrigerant heat exchangers, such as the cascade heat exchanger and the IHX, the same calculation is performed separately for the hot and cold sides.
The following table summarize the optimal geometries and main sizing results of the heat exchangers of the SS+IHX configuration working with Isobutane.

Table 7: Optimized heat exchanger geometries and main sizing results.

| Heat exchanger | $L$ [m] | $W$ [m] | $N_p$ [-] | $A$ [m$^2$] | $\Delta T_{\text{lm,mean}}$ [K] | $V$ [m$^3$] | $U_{\text{mean}}$ [kW/(m$^2$ K)] |
|---|---|---|---|---|---|---|---|
| Evaporator | 1.62 | 0.42 | 600 | 404 | 13 | 0.44 | 1.064 |
| Condenser | 1.32 | 0.22 | 692 | 198 | 25.7 | 0.218 | 1.4 |
| Internal heat exchanger | 2.28 | 0.1 | 621 | 141 | 14 | 0.156 | 0.97 |

## C. Annuity Method

The annuity method used for the economic evaluation is described in this appendix. Its purpose is to convert investment costs, energy costs, and maintenance costs into equivalent annual payments, enabling a consistent comparison of technologies with different cost structures. Capital expenditures are distributed over the evaluation period, while all recurring costs are discounted and annualised on the same annual basis. The resulting annual cost is then used to compute the levelised cost of heat (LCOH).

### Total annuity and LCOH

The total annuity $AN$ represents the equivalent annual cost of the investigated component or system, and is composed of three contributions:

$$AN = AN_K + AN_V + AN_B \tag{54}$$

where:

- $AN_K$ is the *capital-bound annuity*, associated with the initial investment;
- $AN_V$ is the *demand-bound annuity*, related to energy consumption costs;
- $AN_B$ is the *operation-bound annuity*, covering inspection, maintenance, and repair.

The levelised cost of heat of the overall system is obtained by dividing the combined annuity of the heat pump and the auxiliary boiler by the total annual heat delivered to the district heating network:

$$LCOH_{\text{sys}} = \frac{AN_{\text{HP}} + AN_{\text{boiler}}}{Q_{\text{HP}} + Q_{\text{boiler}}} \tag{55}$$

The main economic assumptions adopted in the evaluation are summarized in Table 8.
The annuity factor $a$ converts a present value into an equivalent uniform annual payment over the evaluation period:

$$a = \frac{q^T(q-1)}{q^T - 1} \tag{56}$$

Table 8: Main economic assumptions.

| Parameter | Symbol | Value |
|---|---|---|
| Evaluation period | $T$ | 20 yr |
| Heat pump lifetime | $n_{\text{HP}}$ | 20 yr |
| Boiler lifetime | $n_{\text{boiler}}$ | 20 yr |
| Interest factor | $q$ | 1.0213 |
| Price change factor | $r$ | 1.0131 |
| Mean electricity price | $c_{\text{el}}$ | 133.6 €/MWh |
| Boiler efficiency | $\eta_{\text{boiler}}$ | 0.90 |

## Capital-bound annuity

The project investment cost $C_P$ serves as the basis for the capital-bound annuity. It is obtained by applying material, pressure, temperature, and installation correction factors to the purchased equipment costs. For a generic component $j$:

$$C_{P,j} = \left(f_{M,j}\, f_{P,j}\, f_{T,j} + f_{I,j}\right) C_{i,j} \tag{57}$$

and the total project cost is:

$$C_P = \sum_j C_{P,j} = \sum_j \left(f_{M,j}\, f_{P,j}\, f_{T,j} + f_{I,j}\right) C_{i,j} \tag{58}$$

where $C_{i,j}$ is the purchased equipment cost of component $j$, $f_M$ is the material factor (accounting for corrosion-resistant materials such as stainless steel), $f_P$ is the pressure factor, $f_T$ is the temperature factor, and $f_I = 0.6$ is a uniform installation factor that covers erection, instrumentation, control, and electrical equipment [39].

The correction factors applied to each heat pump component are listed in Table 9.

Table 9: EPC correction factors for the heat pump components.

| Component | $f_M$ | $f_P$ | $f_T$ | $f_I$ |
|---|---|---|---|---|
| Evaporator | 1.7 | 1.5 | 1.6 | 0.6 |
| Condenser | 1.7 | 1.5 | 1.0 | 0.6 |
| Compressor | 1.0 | 1.0 | 1.1 | 0.6 |
| IHX / Cascade HEX | 1.0 | 1.5 | 1.0 | 0.6 |
| Working fluid receiver | 1.0 | 1.5 | 1.0 | 0.6 |
| Working fluid | 1.0 | 1.0 | 1.0 | 0.6 |
| Piping and tanks | 1.0 | 1.5 | 1.0 | 0.6 |
| Boiler | 1.0 | 1.0 | 1.0 | 0.6 |

Given that the heat pump lifetime equals the evaluation period ($n_{\text{HP}} = T = 20$ yr), no replacement investment is required. The capital-bound annuity is therefore:

$$AN_K = A_0\, a \tag{59}$$

where $A_0 = C_P$ is the initial project investment cost.

## Demand-bound annuity ($AN_V$)

The first-year demand-bound cost of the heat pump corresponds to its annual electricity expenditure:

$$A_{V,1,\text{HP}} = c_{\text{el}}\, E_{\text{el,HP}} \tag{60}$$

where $E_{\text{el,HP}}$ is the annual electricity consumption [kWh/a]. More explicitly, the annual electricity cost is obtained from the hourly simulation results as:

$$C_{\text{el}} = \frac{\sum_j \left(P_{\text{shaft,j}} \cdot t_j\right)}{\eta_{\text{el}}} \cdot c_{\text{el}} \tag{61}$$

where $P_{\mathrm{shaft,j}}$ is the compressor shaft power at operating hour $j$, $t_j$ is the corresponding time step, and $\eta_{\mathrm{el}}$ is the electro-mechanical efficiency of the drive equal to 0.95.
For the auxiliary boiler, the analogous first-year cost is determined by the annual natural gas consumption and the corresponding fuel price; the treatment of fuel-related costs and the gas price scenarios considered in this work is described in Section 3.3.
The annual fuel-related cost of the auxiliary boiler is calculated as:

$$C_{\mathrm{fuel}} = \frac{\sum_j \big(\dot{Q}_{\mathrm{boiler,j}} \cdot t_j\big)}{\eta_{\mathrm{boiler}}} \cdot c_{\mathrm{fuel,clean}} \tag{62}$$

where $\dot{Q}_{\mathrm{boiler,j}}$ is the boiler heat duty at hour $j$ and $c_{\mathrm{fuel,clean}}$ is the clean fuel price, defined as:

$$c_{\mathrm{fuel,clean}} = c_{\mathrm{fuel}} + EF_{\mathrm{fuel}} \cdot c_{\mathrm{EUA}} \tag{63}$$

Here $EF_{\mathrm{fuel}}$ is the emission factor of natural gas and $c_{\mathrm{EUA}}$ is the cost of $CO_2$ emission allowances under the EU ETS. The gas price scenarios and $CO_2$ cost levels considered in this work are detailed in Section 3.3.
To account for the time value of money and anticipated price escalation, recurring annual costs are discounted using the price-dynamic cash-value factor $b_V$:

$$b_V = \begin{cases} \dfrac{T}{q}, & r = q \\ \dfrac{1 - \big(r/q\big)^T}{q - r}, & r \neq q \end{cases} \tag{64}$$

where $q$ is the interest factor and $r$ is the price change factor (see Table 8). The demand-bound annuity is then:

$$AN_V = A_{V,1}\, b_V\, a \tag{65}$$

### Operation-bound annuity ($AN_B$)

Operation-bound costs comprise inspection, maintenance, and repair. Following the VDI 2067 guideline [42], these are assumed proportional to the initial project investment:

$$A_{IN,\mathrm{HP}} = A_0\big(f_{\mathrm{insp}} + f_{\mathrm{maint}}\big) \tag{66}$$

For heat pumps, the VDI 2067 guideline prescribes $f_{\mathrm{repair}} = 1\,\%$ and $f_{\mathrm{s+i}} = 1.5\,\%$, giving a combined rate of 2.5 % of the project investment per year.
The operation-bound annuity is obtained by applying the same price-dynamic cash-value factor $b_V$ defined in Eq. (64):

$$AN_B = A_{IN,\mathrm{HP}}\, b_V\, a \tag{67}$$

# Appendix nomenclature

### Acronyms

| | |
|---|---|
| BVR | Built-in Volume Ratio |
| EPC | Engineering, Procurement and Construction |
| EUA | EU Emission Allowance |

### Physical quantities

| | |
|---|---|
| $a$ | Annuity factor |
| $A$ | Heat transfer area, $\mathrm{m^2}$ |
| $A_0$ | Initial project investment, € |
| $a_m$ | Corrugation amplitude, m |
| $A_p$ | Plate heat transfer area, $\mathrm{m^2}$ |
| Bo | Boiling number |
| $b_V$ | Price-dynamic cash-value factor |
| $C_P$ | Project investment cost, € |
| $d_h$ | Hydraulic diameter, m |
| $d_p$ | Plate spacing, m |
| $E$ | Annual energy, kWh/a |
| $f_I$ | Installation factor |
| $f_M$ | Material factor |
| $f_P$ | Pressure factor |
| $f_T$ | Temperature factor |
| EF | Emission factor of natural gas |
| $k_{wall}$ | Wall thermal conductivity, kW/(m K) |
| $L$ | Plate length, m |
| Nu | Nusselt number |
| $N_p$ | Number of plates |
| $n_{ref}$ | Reference rotational speed, Hz |
| $q$ | Interest factor |
| $\dot{q}$ | Heat flux density, $\mathrm{kW/m^2}$ |

### Physical quantities

| | |
|---|---|
| Re | Reynolds number |
| $r$ | Price change factor |
| $R_f$ | Fouling resistance, $\mathrm{m^2\,K/kW}$ |
| $r_p$ | External pressure ratio |
| $r_v$ | Applied volume ratio |
| $r_{v,p}$ | Volume-to-pressure ratio |
| $t$ | Time step, h |
| $T$ | Evaluation period, yr |
| $U$ | Overall heat transfer coeff., $\mathrm{kW/(m^2\,K)}$ |
| $\dot{V}$ | Volumetric flow rate, $\mathrm{m^3/s}$ |
| $V_{ch}$ | Channel volume, $\mathrm{m^3}$ |
| $W$ | Plate width, m |
| $\alpha$ | Convective heat transfer coeff., $\mathrm{kW/(m^2\,K)}$ |
| $\Delta p$ | Pressure drop, bar |
| $\Delta T_{lm}$ | Log-mean temperature difference, K |
| $\eta_{is}$ | Isentropic efficiency |
| $\eta_{vol}$ | Volumetric efficiency |
| $\lambda$ | Thermal conductivity, kW/(m K) |
| $\Lambda$ | Corrugation wavelength, m |
| $\varphi$ | Chevron angle, ° |
| $\xi$ | Friction factor |

### Subscripts

| | |
|---|---|
| 0 | Reference value |
| ch | Channel |
| cold | Cold side |
| flow | Flow (cross-section) |
| fuel | Natural gas fuel |
| hot | Hot side |
| IN | Inspection / maintenance |
| $j$ | Component / time-step index |
| K | Capital-bound |
| B | Operation-bound |
| V | Demand-bound |
| mean | Mean value |
| $N$ | Normalised |
| req | Required |
| suc | Compressor suction |

# Abstract in lingua italiana

La decarbonizzazione del settore del riscaldamento rappresenta una delle principali sfide della transizione energetica, e le pompe di calore ad alta temperatura integrate nelle reti di teleriscaldamento costituiscono una soluzione promettente per la riduzione delle emissioni di gas serra. Il presente lavoro analizza la fattibilità tecnico-economica dell'integrazione di una pompa di calore ad alta temperatura in un sistema geotermico situato nella Valle dell'Isar. Sono state considerate tre configurazioni di ciclo: un ciclo a singolo stadio, un ciclo a singolo stadio dotato di scambiatore di calore interno (IHX) e un ciclo a cascata a due stadi. Per ciascuna configurazione è stata effettuata una selezione preliminare di fluidi refrigeranti a basso potenziale di riscaldamento globale, unitamente alla determinazione della minima taglia del compressore necessaria a coprire il picco della domanda termica.

Le prestazioni sono state valutate mediante simulazioni termodinamiche annuali condotte in condizioni operative realistiche, integrate da un'analisi di scalabilità nella quale la potenza installata della pompa di calore viene progressivamente ridotta e il carico residuo viene coperto da una caldaia ausiliaria alimentata a gas naturale.

Le diverse configurazioni sono state confrontate attraverso indicatori termodinamici ed economici, quali il coefficiente di prestazione, il consumo energetico annuale, le ore equivalenti di funzionamento, il costo livellato del calore e il Payback time. Tra le configurazioni analizzate, il ciclo a singolo stadio con scambiatore di calore interno ha evidenziato le migliori prestazioni dal punto di vista tecnico-economico. I refrigeranti idrocarburici hanno fornito i risultati complessivamente più favorevoli: in particolare, l'isobutano ha consentito di ottenere il più basso valore preliminare di LCOH, pari a 77.5 €/MWh, con un COP al punto di progetto pari a 4.45 e una differenza di temperatura ottimale nel recuperatore di 11 K, risultante dal compromesso tra il miglioramento dell'efficienza del ciclo e l'incremento dei costi di investimento.

L'analisi economica mostra che il valore minimo del LCOH di sistema si ottiene per bassi fattori di dimensionamento; tuttavia, considerando congiuntamente il LCOH, la quota di energia rinnovabile fornita alla rete e le ore equivalenti di funzionamento, un fattore di dimensionamento pari a circa 0.6 rappresenta il compromesso più vantaggioso, consentendo di coprire l'89% della domanda termica annuale. Un'analisi di sensibilità evidenzia che la dimensione economicamente ottimale della pompa di calore è governata dal rapporto tra il prezzo del gas naturale e quello dell'energia elettrica, spostandosi verso taglie maggiori all'aumentare del costo del gas rispetto all'elettricità, mentre il fattore di dimensionamento selezionato si conferma una scelta robusta grazie alla limitata variazione del LCOH in prossimità del suo minimo. Il Payback time attualizzato dell'investimento conferma la medesima graduatoria, con il ciclo a singolo stadio dotato di IHX che ammortizza l'investimento in 18 anni in condizioni di prezzo di riferimento, riducendosi a circa 5 anni in presenza di un prezzo della $CO_2$.

**Parole chiave:** Pompe di calore ad alta temperatura, Refrigeranti a basso GWP, Dimensionamento del compressore, Valutazione Tecnico-Economica, Costo livellato del calore (LCOH)